

Scale Invariance in Liquid Water Distributions in Marine Stratocumulus. Part II: Multifractal Properties and Intermittency Issues

ALEXANDER MARSHAK,* ANTHONY DAVIS,* WARREN WISCOMBE, AND ROBERT CAHALAN

Climate and Radiation Branch, NASA/Goddard Space Flight Center, Greenbelt, Maryland

(Manuscript received 2 June 1995, in final form 5 August 1996)

ABSTRACT

This is the second of two papers analyzing the internal liquid water content (LWC) structure of marine stratocumulus (Sc) based on observations taken during the First ICCP (International Commission on Cloud Physics) Regional Experiment (FIRE) 1987 and Atlantic Stratocumulus Transition Experiment (ASTEX) 1992 field programs. Part I examined wavenumber spectra and the three-decade scale range (tens of meters to tens of kilometers) over which scale invariance holds; the inability of spectral analysis to distinguish between different random processes was also underscored. This indetermination is removed in this part by applying multifractal analysis techniques to the LWC fields, leading to a characterization of the role of intermittency in marine Sc.

Two multiscaling statistics are computed and associated nonincreasing hierarchies of exponents are obtained: structure functions and $H(q)$, singular measures and $D(q)$. The real variable q is the order of a statistical moment (e.g., $q = 1.0$ yields a mean); $D(q)$ quantifies intermittency, $H(q)$ nonstationarity. Being derived from the slopes of lines on log(statistic) versus log(scale) plots, these exponents are only defined when those lines are reasonably straight and where this happens defines the scale-invariant range. Being nonconstant, the derived $H(q)$ and $D(q)$ indicate multifractality rather than monofractality of LWC fields.

Two exponents can serve as first-order measures of nonstationarity and intermittency: $H_1 = H(1)$ and $C_1 = 1 - D(1)$. For the ensemble average of all FIRE and all ASTEX data, the authors find the two corresponding points in the (H_1, C_1) plane to be close: (0.28, 0.10) for FIRE and (0.29, 0.08) for ASTEX. This indicates that the dynamics determining the internal structure of marine Sc depend little on the local climatology. In contrast, the scatter of spatial averages for the individual flight around the ensemble average illustrates ergodicity violation. Finally, neither multiplicative cascades (with $H_1 = 0$) nor additive Gaussian models such as fractional Brownian motions (with $C_1 = 0$) adequately reproduce the LWC fluctuations in marine Sc.

1. Introduction

In this second paper of a two part series, we continue to investigate the statistical properties of liquid water content (LWC) spatial structure in marine stratocumulus (Sc) and enlarge the data analysis toolbox beyond the usual Gaussian moments, autocorrelation functions, variograms, and/or power spectra. Davis et al. (1996a), hereafter referred to as Part I, emphasized scale-invariant (“scaling”) ranges and addressed stationarity issues from the standpoint of Gaussian statistics and spectral analysis. This part emphasizes multifractal statistics and the role of intermittency.

Our database consists of LWC time series collected by aircraft during the First ICCP (International Commission on Cloud Physics) Regional Experiment (FIRE)

and Atlantic Stratocumulus Transition Experiment (ASTEX) field programs. FIRE (phase I) was conducted in summer 1987 (hereafter FIRE 87) off the coast of Southern California (Albrecht et al. 1988), largely in solid stratocumulus; ASTEX (FIRE phase II) was conducted in summer 1992 in a broad area around the Azores Islands, in conditions varying from solid to broken stratocumulus (Albrecht et al. 1995). The ASTEX LWC data was described by Davis et al. (1994a); the FIRE 87 LWC data in Part I. Figures 1a–e illustrate representative portions of this data and Table 1 itemizes the important parameters of the five FIRE 87 datasets, reproduces selected results from Part I, and summarizes some of our findings.

In Part I we found that both FIRE 87 and ASTEX LWC are statistically “scale invariant” in the sense that their ensemble-average wavenumber spectra follow power laws: $E(k) \propto k^{-\beta}$ where the spectral exponents β were found to be very close; 1.36 ± 0.06 for FIRE and 1.43 ± 0.08 for ASTEX. The corresponding “scaling” ranges are both three decades long but offset: 20 m to at least 20 km for FIRE, 60 m to at least 60 km for ASTEX. The lower end of the scaling range for FIRE is nearly at the resolution of the data and so may not

*Additional affiliation: Science Systems and Applications, Inc., Lanham, Maryland.

Corresponding author address: Dr. Alexander Marshak, NASA/GSFC, Code 913, Greenbelt, MD 20771.
E-mail: marshak@climate.gsfc.nasa.gov

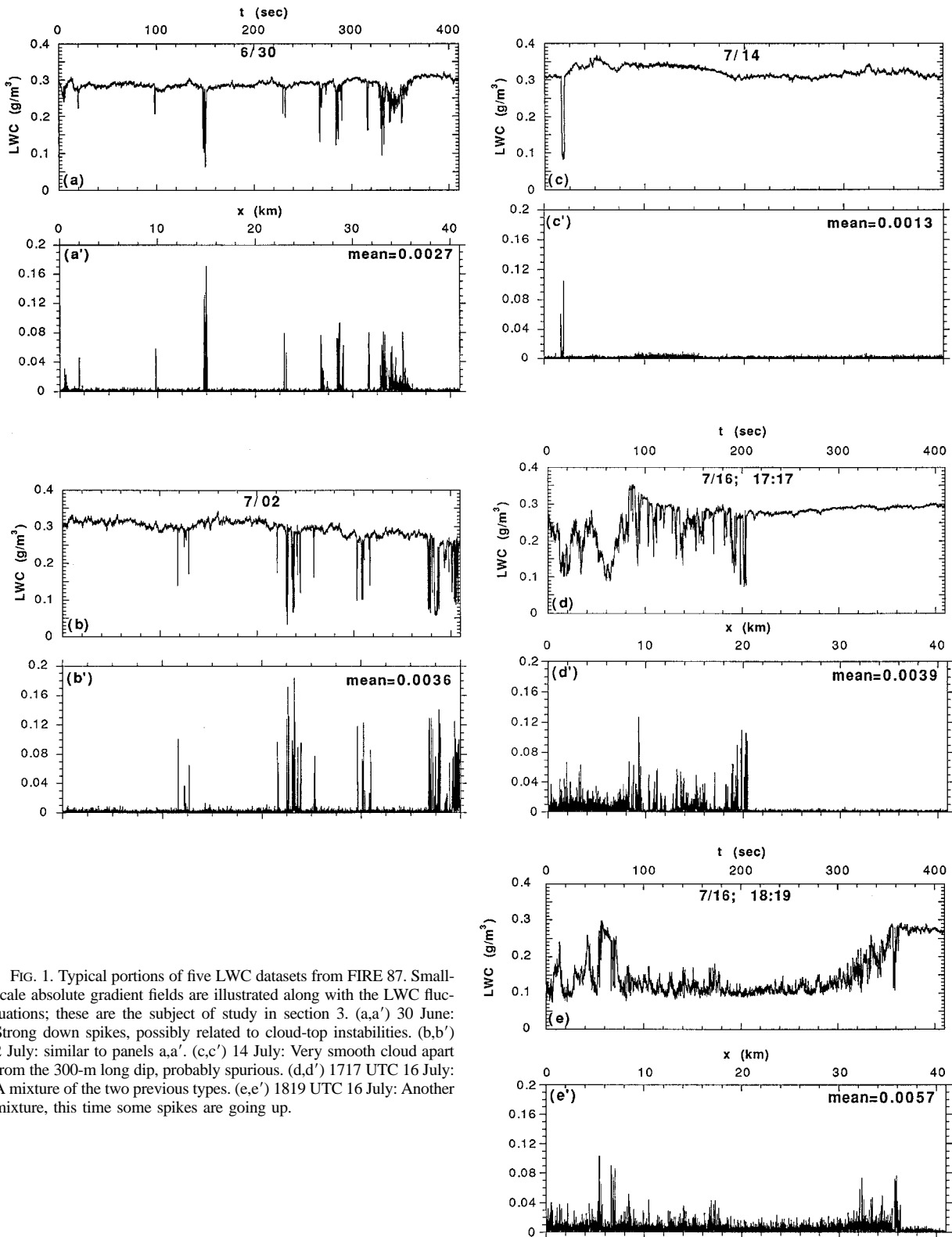


FIG. 1. Typical portions of five LWC datasets from FIRE 87. Small-scale absolute gradient fields are illustrated along with the LWC fluctuations; these are the subject of study in section 3. (a,a') 30 June: Strong down spikes, possibly related to cloud-top instabilities. (b,b') 2 July: similar to panels a,a'. (c,c') 14 July: Very smooth cloud apart from the 300-m long dip, probably spurious. (d,d') 1717 UTC 16 July: A mixture of the two previous types. (e,e') 1819 UTC 16 July: Another mixture, this time some spikes are going up.

TABLE 1. Characteristics and statistical properties of the FIRE '87 (King probe) LWC datasets. Measurements were made during the FIRE 1987 stratocumulus experiment, off San Diego, California. A nominal aircraft speed of 100 m s^{-1} was used for the time-to-space conversion, the sampling rate being 20 Hz. Results for the spectral exponents (β_{LWC} and β_ϵ) are being reproduced from Part I; the other exponents are obtained by the methods explained in the text. Arrows indicate columns that are constrained by Wiener–Khinchine relations. For the nonstationary LWC data itself, $\beta = \zeta(2) + 1$ is verified in every case, generally well within the typical uncertainties on the exponents (0.03–0.08). The wavenumber spectra of the small-scale absolute gradient fields ϵ_{LWC} do not scale well enough individually to define exponents but their ensemble average does; cf. Part I (Fig. 10).

Date (1987)	Time (PDT)	N_{tot} (points)	$\log_2 N_{\text{tot}}$	L (km)	Type	$\zeta(1)$ $= H_1$	$K'(1)$ $= C_1$	$\zeta(2)$ ↓	$K(2)$	β	
										LWC ↓	ϵ_{LWC}
30 Jun	2241	28 672	14.81	143	spiky	0.29	0.14	0.41	0.25	1.39	
2 Jul	0223	16 384	14	82	spiky	0.22	0.15	0.22	0.25	1.19	
14 Jul	2309	65 536	16	328	smooth	0.34	0.03	0.67	0.06	1.68	
16 Jul	1717	8192	13	41	mixed	0.31	0.08	0.42	0.19	1.47	
16 Jul	1819	12 020	13.55	60	mixed	0.34	0.07	0.55	0.12	1.53	
Totals		130 804		654							
Ensemble averages						0.28	0.10	0.37	0.21 ↑	1.36	≈ 0.7 ↑

be meaningful, but for ASTEX the instrumentation had better spatial resolution and the scale break at 60 m is not only robust but an as yet unexplained result.

The main advantage of spectral analysis is that a wavenumber spectrum can be defined for any stochastic process $\varphi(x)$, whether statistically stationary or not. “Stationarity” is statistical invariance property, in this case, under translation in x . More precisely, stationarity requires that the autocorrelation function $\langle \varphi(x+r)\varphi(x) \rangle$ should be a function of r only. We use $\langle \cdot \rangle$ to designate an ensemble or φ average, but in practice we always compute statistics by using a spatial or x average. This means that we end up postulating some form of “ergodicity,” that is, the convergence of the two types of average for large samples. Since ergodic processes are a subclass of stationary ones, it is convenient to have an operational criterion for stationarity. In Part I we show that this is possible in the framework of scale invariance: $\beta < 1$ (for more details, see Davis et al. 1996b). As an illustration of nonstationary behavior, we showed that such common statistics as mean and standard deviation are highly unstable for LWC. Only at scales outside of the nonstationary scaling regime is some degree of convergence observed.

This strength of spectral analysis is offset by its ambiguity as an indicator of structure; we recall that very different looking processes can have identical spectra. For instance, white noise (a sequence of uncorrelated random numbers) has $E(k) = \text{constant}$ but so do randomly positioned δ functions. The role of the multifractal approaches used here is to extract more structural information from the data by importing the notion of intermittency from turbulence. Spectral analysis was developed largely for engineering-type problems, such as signal processing with linear circuitry. In this context, being only a second-order statistic is not a major limitation; the signals of interest are assumed to be Gaussian, defined entirely by their means, variances, and covariances. In contrast, multifractal analysis is rooted in

the nonlinear physics of natural phenomena. By considering higher-order statistics, it complements the spectral approach.

Hardly a decade after their inception (Grassberger 1983; Hentschel and Procaccia 1983; Parisi and Frisch 1985), multifractal concepts have proven invaluable in nonlinear science. Their better-known applications are deterministic chaos (Ott 1993) and turbulence (Sreenivasan 1991). As a general framework for statistical analysis and stochastic simulation of natural phenomena, new applications of multifractals are appearing on a regular basis. Also, it is important to note that multifractal analysis can be reformulated (Davis et al. 1994b and references therein) and generalized (Muzy et al. 1993) within the framework of wavelet transforms.

Multifractals have been used in several areas of meteorological interest, rain rate variability being the most successful application to date (Gupta and Waymire 1993 and references therein). Professor Lovejoy’s group at McGill University is making steady progress on the earth’s radiation fields at various wavelengths (Gabriel et al. 1988; Tessier et al. 1993). Recent theoretical cloud radiation studies have involved both fractal models (Gabriel et al. 1990; Davis et al. 1990; Barker and Davies 1992) and multifractal models (Cahalan 1989; Davis et al. 1991a,b; Evans 1993a,b; Cahalan et al. 1994a,b; Marshak et al. 1995a,b; Davis et al. 1997).

This paper is organized as follows. Section 2 describes structure functions in the framework of scale invariance considering statistics of all orders. In section 3 we turn to singular measures, the simplest incarnation of singularity analysis. In section 4 structure functions are interpreted as a means of quantifying and qualifying nonstationarity in cloud structure; singular measures play the same role for intermittency. For both multifractal approaches, we discuss spurious scaling and/or breaks in scaling due to glitches in the data and/or insufficient sampling, detail the scaling of the results for FIRE 87 data, and compare their end products (expo-

nents, prefactors, and scaling ranges) with those of AS-TEX. In section 5 we use the “bifractal plane,” a simple two-parameter representation of nonstationary and/or intermittent geophysical data, to discuss ergodicity violations in FIRE 87 marine Sc and the status of stochastic cloud modeling. We draw our conclusions and outline some developments and applications in section 6. Interpretation of selected multifractal statistics in terms of fractal geometry is discussed in the appendix.

2. The q th-order structure functions of LWC in marine Sc

a. Generalities and practicalities of structure functions

Although our focus is the variability of LWC in marine Sc, the techniques we use are applicable to any dataset representative of a geophysical field. In an effort to make multifractal statistics more palatable, we will describe them in general terms. We assume, given at least one large one-dimensional sequence of scalar quantities,

$$\varphi_i = \varphi(x_i), \quad x_i = i\ell \quad (i = 1, \dots, N_{\text{tot}}), \quad (1)$$

a discretized version of the random process $\varphi(x)$, $0 \leq x \leq L$ (with $N_{\text{tot}} = L/\ell \gg 1$). We first assume this field is scale invariant; its energy spectrum follows a power law,

$$E(k) \propto k^{-\beta}, \quad (2)$$

over a large range of k from which a range of scales ($r = 1/k$) can be deduced. We further assume it is nonstationary ($\beta > 1$) with stationary increments ($\beta < 3$). The statistical properties of the increments

$$\Delta\varphi(r; x) = \varphi(x+r) - \varphi(x), \quad 0 \leq r \leq L, \\ 0 \leq x \leq L-r \quad (3)$$

will therefore be independent of position x . This applies in particular to $\langle |\Delta\varphi(r; x)|^q \rangle \equiv \langle |\Delta\varphi(r)|^q \rangle$, the structure function of order q . Due to the scale invariance, we expect

$$\langle |\Delta\varphi(r)|^q \rangle \propto r^{\zeta(q)}, \quad q \geq 0, \quad (4)$$

where $\langle \cdot \rangle$ denotes an ensemble average. Extension of this statistic for $q < 0$ is discussed by Muzy et al. (1993). Finally, we assume that there is a large range of r -values where the power law relations (4) apply for all the q of interest.

Some general statements can be made about $\langle |\Delta\varphi(r)|^q \rangle$ and $\zeta(q)$ as functions of q . First, proper normalization in (4) requires $\zeta(0) = 0$. Furthermore, $\zeta(q)$ is a concave function (Parisi and Frisch 1985) and it is also nondecreasing if the increments in Eq. (3) are bounded (Frisch 1991; Marshak et al. 1994). We can therefore define the hierarchy of exponents:

$$H(q) = \frac{\zeta(q)}{q}, \quad q \geq 0. \quad (5)$$

By “hierarchy” we mean a monotonic function, in this

case, nonincreasing. Narrowly distributed increments, “short-tailed” according to Waymire and Gupta’s (1981) classification, are a special but important case: we have $\langle |\Delta\varphi(r)|^q \rangle \approx \langle \Delta\varphi(r)^2 \rangle^{q/2}$. Equations (4)–(5) then yield $\zeta(q) = q\zeta(2)/2$, hence $H(q) \equiv H(2)$; one exponent determines the scaling of all the moments of the increments. This is called “monoscaling”; if $\zeta(q)$ is not linear in q , we talk about “multiscaling.”

At least two $\zeta(q)$ are well known. For nonstationary scaling processes with stationary increments, the Wiener–Khinchine theorem reads as (Monin and Yaglom 1975)

$$1 < \beta = \zeta(2) + 1 = 2H(2) + 1 < 3. \quad (6)$$

Structure-function analysis at all orders is therefore a complement to spectral analysis, applicable primarily to nonstationary signals. Furthermore,

$$0 < H_1 = H(1) = \zeta(1) < 1 \quad (7)$$

is the “roughness” or Hurst exponent that we will use to characterize the nonstationarity of the data. The upper limits in Eqs. (6)–(7) corresponds to nonconstant everywhere differentiable signals, which yield $|\Delta\varphi(r; x)| \propto r$ for almost all x and φ [see Eq. (4) with $q = 1$, as well as the appendix].

b. Test case

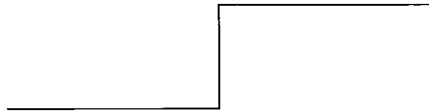
What if our specific dataset does not lead to the simple straight line when plotting $\langle |\Delta\varphi(r)|^q \rangle$ versus r in log–log axes? What if it is easier to see two or more scaling regimes? Can we conclude that there is a break in the scaling?

Before assigning $\zeta(q)$ to marine Sc LWC, we address these basic issues with the help of a short time series ($N = 2^{10}$ points, $L = N\ell$, $\ell = 1$) borrowed from the 14 July 1987 FIRE LWC dataset rearranged for tutorial purposes (Fig. 2a). A priori, here are three special scales, r_1 , r_2 , and r_3 . The first two ($r_1 \approx 2^4$ and $r_2 \approx 2^6$) correspond to the widths of the first (deepest) and second (shallower) dips, while the third ($r_3 \approx 2^8$) is the distance between them. The latter actually belongs to the dataset (Fig. 1c), the former is artificial. We now show why the corresponding structure functions (Fig. 2b) cannot be described by a single power law in r .

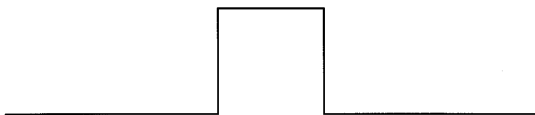
Consider the largest q ($q = 5$, reproduced from Fig. 2b in Fig. 2c); this choice emphasizes the most intense events. As r increases, the fifth-order structure function first increases sharply because the increments from the top to the bottom of the deeper dip (width r_1) dominate and there are more and more of these. Then $\langle |\Delta\varphi(r)|^5 \rangle$ is “saturated” with respect to this dip; for all $r \geq r_1$, $|\Delta\varphi(r)|^5$ contributes a fixed number of events to the spatial average. Further on, we see the secondary dip (width r_2) at work in a similar way. It allows $\langle |\Delta\varphi(r)|^5 \rangle$ to keep growing but at a slower rate because smaller increments are spawned by this structure. For $r \geq r_2$, the fifth-order structure function has again become saturated. We can thus retrieve two of our special

scales, r_1 and r_2 , from a close look at $\log\langle|\Delta\varphi(r)|^q\rangle$ (for large q), looking for r values where the slopes change. The last remarkable scale is r_3 . We see the deficit in $\langle|\Delta\varphi(r)|^5\rangle$ at this point. However, for the purposes of this tutorial, r_3 was set to 2^8 so that our sampling of the parameter r by powers of 2 would not miss it.

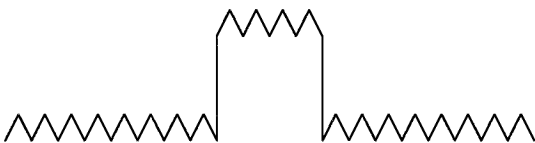
The slopes of $\zeta(q)$ can be predicted only in some simple theoretical cases. As shown above, Heaviside-type step functions



produce straight lines over all scales with $\zeta(q)$ equal to unity for $q > 0$. For a piece-wise constant hat function



of width r^* , the slopes are equal to unity for all $r \leq r^*$ and 0 otherwise ($q > 0$). Imagine a weakly variable function superimposed on the hat function



then, instead of being independent of q , the slopes are equal to unity for large q only, when the increments due to the small fluctuations become statistically negligible with respect to those caused by the anomaly. Furthermore, if the signal around the bump goes up or down gradually



then the large q slopes emphasize the details of the rise to and descent from the high part of the dataset. This is qualitatively what we see in Figs. 2b,c.

Looking back to Fig. 2b, we can focus on typical rather than extreme increments by choosing $q = 1$. Since we see no more break in the scaling at r_1 , we know that these numerous lesser but more average increments overwhelm the contributions, however large, due to the first dip. Specifically, we find a slope, $H_1 \approx 0.7$, which tells us that, ignoring the dips, this signal is rather smooth. The localized effect of r_3 is also imperceptible. If the break in scaling, say, at r_1 had persisted down to $q = 1$, our conclusions would be quite different. We would have grounds to say

that structures at scale r_1 are frequent enough to influence the mean behavior and, in all likelihood, these would be visually prominent in the data. However, there is no guarantee that such a break in scaling will survive averaging over several datasets collected in conditions similar enough to view them as a statistically homogeneous whole. Examples will follow.

Still focusing on $q = 1$, the second dip (width $r_2 \approx 2^6$) cannot break the scaling for the same reasons invoked at r_1 ; the saturation of $\langle|\Delta\varphi(r)|\rangle$ at $\log_2 r \approx 6$ occurs for another reason. In this case we observe that the mean increments no longer increase because the portion of data chosen for this exercise is relatively flat (apart from the two dips, inconsequential at $q = 1$). For large enough r , we always expect stationary-type (r -independent) structure functions. We simply have nonstationary behavior for $r \leq 2^6$ and stationary behavior for $r \geq 2^6$; the crossover defines the integral correlation scale R .

As we will see, 2^6 turns out to be an underestimate of the crossover scale R and this small portion of 14 July data can only be viewed as pseudostationary at scales $2^6 \leq r \leq 2^9$. This last value marks the transition to scale independence for $\langle|\Delta\varphi(r)|^q\rangle$ using the whole dataset. At the same time, $H_1 \approx 0.7$ is a gross overestimate with respect to the complete dataset. This is a good example of how nonstationary data are also nonergodic, that is, how single spatial averages cannot be representative of a whole atmospheric process. In this case, R is underestimated and H_1 is overestimated because the data is locally smoother than average; apart from the dips, the data in Fig. 2a is stationary over the relatively wide range of scales that we can assess visually.

All of the above statistical idiosyncrasies are traceable to sampling problems and occur for some of the LWC datasets in section 2c. We would draw erroneous conclusions if we were to consider the longest dataset (14 July) as the most representative since it also happens to be the smoothest of the set.

c. Results for LWC in marine Sc for FIRE 87

Let us summarize:

- However random data may look, it generally has recognizable patterns or structure; q th-order structure functions provide us with a simple statistical tool to study these recurrent patterns.
- If only one dataset is available, we must make an ergodicity assumption to estimate ensemble averages. This assumption is generally not valid for extreme events, however, and related breaks in scale invariance cannot be considered robust or physical without further confirmation.
- If several datasets that form a statistically homogeneous whole are available, then the influence of the ergodicity assumption can be minimized by averaging the statistics over all of them.

We recall from Part I that there are three types of

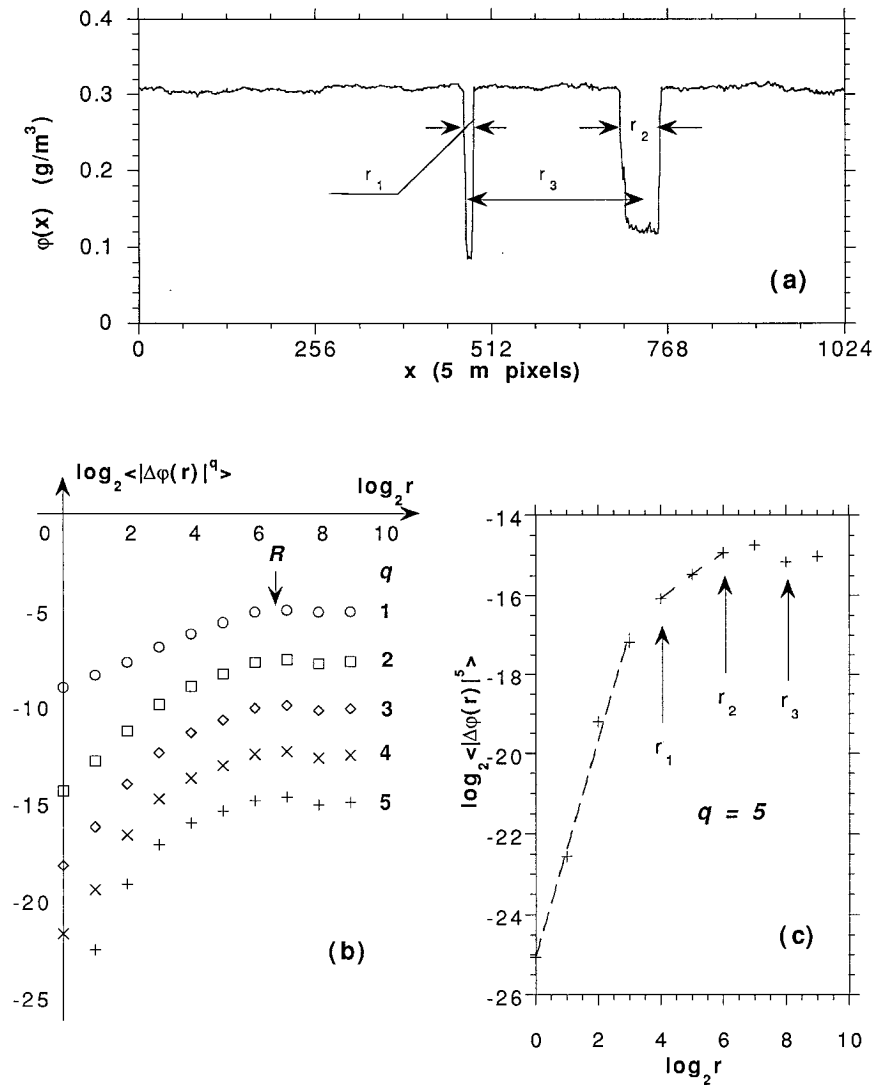


FIG. 2. Test data and q th-order structure function analysis. (a) LWC data $\phi(x)$, $0 \leq x \leq 1024$, extracted from the 14 July run, partially reproduced in Fig. 1c. This data contains the suspicious glitch described in Part I and a narrower, stronger dip has been added in front of it for tutorial purposes. Three characteristic scales are highlighted. (b) Scaling of the structure functions $\langle |\phi(x+r) - \phi(x)|^q \rangle$ for $\log_2 r = 0(1)9$ with $\ell = 1$ and $q = 1(1)5$, displaced for clarity. The leveling off at $r \approx 2^6$ is a manifestation of “pseudo-stationarity” in this small portion of nonstationary data (see text). (c) Same as (b) but for $q = 5$ in order to single out the most intense events, allowing us to identify three special scales in the data.

data in our collection. The 30 June and 2 July flights (Figs. 1a,b) exhibit interesting variability with deep sporadic downward spikes. The 14 July flight (Fig. 1c) appears to be through a very homogeneous cloud layer but contains an anomaly, a deep dip lasting 3 s, or 60 pixels (300 m) long. The two flights on 16 July (Figs. 1d,e) are a mixture of the previous two types. Figures 3–5 show our estimates of $\langle |\Delta\phi(r)|^q \rangle$ versus r in log–log (base 2) axes for $1 \leq q \leq 5$; r is reckoned in 5-m pixels so its range is from $\ell = 1$ to the largest power of 2 less or equal to $L/2 = N_{\text{tot}}/2$ (cf. Table 1). For all of these r values, at least $N_{\text{tot}}/2$ two-point events con-

tribute to the spatially averaged structure functions. Our aim is to obtain the individual and ensemble $\zeta(q)$ and associated scaling range $[\eta, R]$ if different from $[\ell, L]$. First we consider each flight separately.

Figure 3 is devoted to the 14 July data. In (a) the second half of the dataset is used (half of which is illustrated in Fig. 1c). There is a clear break in scaling for $q \geq 2$ around $\log_2(r/\ell) = 6$, the size of the conspicuous dip in Fig. 1c. In (b) the dip is avoided by starting the average after the dip; the scaling is indeed restored, up to $r/\ell = 2^{12}$ where the increments no longer increase; equivalently, stationary behavior sets in. This gives us an estimate of the integral

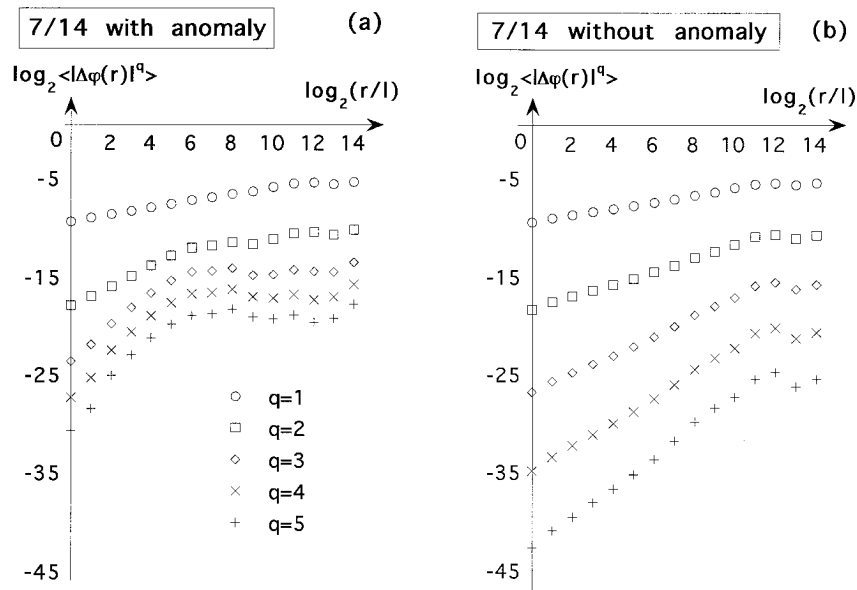


FIG. 3. Structure functions for the “smooth” 14 July LWC dataset from FIRE 87, with and without anomalies. (a) First panel shows $\log_2\langle|\Delta\phi(r)|^q\rangle$ vs $\log_2(r/l)$ for the second half of the flight for $q = 1(1)5$, top to bottom. Notice the saturation at $r \approx 2^6\ell$, the width of the dip visible in Fig. 1c. (b) The same statistics after moving the beginning of the sample to after the dip. Saturation now occurs at the integral scale ($\approx 2^{12}$ pixels, 20 km), where stationary behavior sets in.

scale in marine Sc during FIRE 87 of 20 km. The slopes $\zeta(q)$ are determined by regression without the largest and more stationary scales and are plotted in Fig. 6. They follow closely $\zeta(q) \approx qH_1$ with $H_1 \approx 1/3$. This gives us Kolmogorov (1941) scaling for the energy spectrum: $\beta \approx 5/3$ from Eq. (6), consistent with the direct Fourier transform estimate.

The 30 June and 2 July datasets’ structure functions are plotted in Figs. 4a and 4b, respectively. The traceable breaks in the scaling are due to extreme events in both cases, although this time there is no question of being anomalous. The average $\langle|\Delta\phi(r)|^q\rangle$ s for the two flights in Fig. 4c scale well from $\log_2(r/\ell) = 2$ (20 m) to $\log_2(r/\ell) = 10$ (5 km). Figure 4d shows the average for the two 16 July flights where the upper bound of the scaling range extends to $\log_2(r/\ell) = 12$ (20 km). The exponents associated with moments of order $0 \leq q \leq 5$ for the first (30 June, Fig. 1a) and last (16 July, 1819 UTC, Fig. 1e) flights are plotted in Fig. 6. In Table 1 we show that $\beta \approx \zeta(2) + 1$ in all cases, an independent confirmation of the hypothesis of nonstationarity with stationary increments.

In sharp contrast with the exponents for 14 July (without the anomalous dip), we notice the nonlinearity of $\zeta(q)$ with respect to q . Given the large range of scales involved, these LWC fields are endowed with multifractality. Not surprisingly, the intermittent, spiky 30 June is the most multifractal. All of the general features of the $\zeta(q)$ function described in section 2a are observed, including monotonicity. Notice the increase in fractal graph dimension (cf. the appendix), hence more jumpiness, and the decrease in spectral exponent in Eq. (6), hence more high-frequency

energy, with the multifractality of the cloud, as measured by the curvature in its $\zeta(q)$ function.

d. Comparison of average structure functions for FIRE 87 and ASTEX

In Fig. 5 we show $\langle|\Delta\phi(r)|^q\rangle$ averaged over all five datasets for the first five integer values of q and r up to 40 km (2^{13} pixel), after which the shorter datasets (30 June, 2 July, and 16 July) no longer contribute and the longest (14 July) shows evidence of stationary behavior. The scaling is fairly good from 20 km down to 20 m; the corresponding exponents are highlighted in Fig. 6. For small q , the exponents $\zeta(q)$ corresponding to the average over all five datasets are close to the weighted average over the exponents. For example, the $H_1 = \zeta(1)$ for each dataset is displayed in Table 1. Their average, weighted by L , is 0.31 while the H_1 from the scaling of $\langle|\Delta\phi(r)|^q\rangle$ averaged over all datasets (Figs. 5 and 6) is 0.28. Increasing q , the situation becomes quite different: rougher datasets (30 June and especially 2 July) dominate the average. This is because, in spite of their large number, the smaller increments (smoother data) contribute little to higher-order moments.

Finally, we have reproduced in Fig. 6 the $\zeta(q)$ values obtained by Davis et al. (1994a) for an average over five LWC datasets captured by H. Gerber during ASTEX in June 1992. These datasets were selected from among many others to be “in cloud” for as long as possible ($L \approx 130$ km) to make the comparison with FIRE 87 data meaningful. A slightly slower sampling rate was used than in

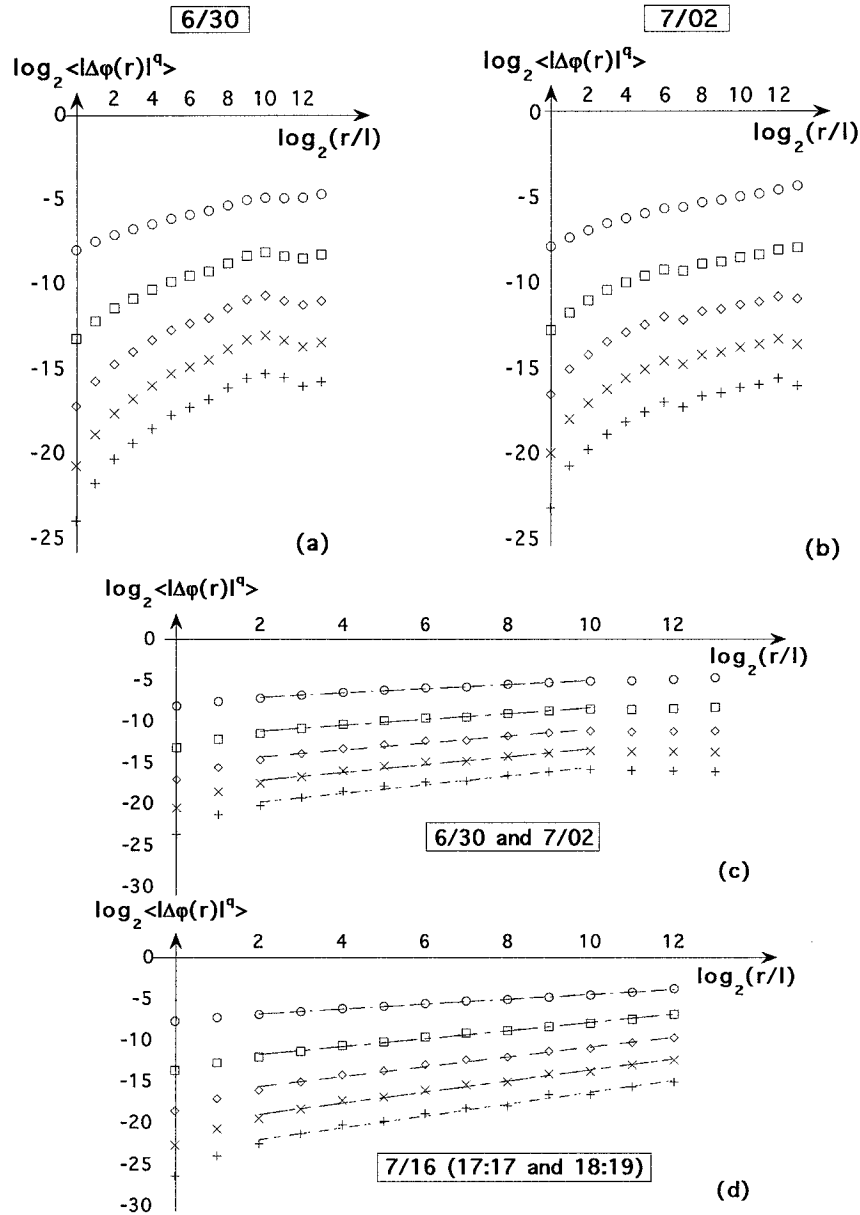


FIG. 4. Structure functions for the “rougher” LWC datasets from FIRE 87, before and after averaging. Same as Fig. 3 except (a) for the 30 June flight and (b) for the 2 July flight (Figs. 1a,b). (c) The average of the two datasets in (a) and (b). (d) The average of the 1717 UTC and 1819 UTC 16 July datasets (Figs. 1d,e).

FIRE 87 (10 Hz for an aircraft speed of ≈ 80 m/s, $\ell \approx 8$ m). The two $\zeta(q)$ functions agree for the smallest q , representative of “typical” increments: relatively small and well sampled. The agreement of the exponents up to $q \approx 1.5$ argues for common features in the internal distributions of liquid water in marine Sc; their corresponding statistical properties depend little on local climatology. The FIRE 87 and ASTEX exponents differ for larger q ; the more pronounced curvature in $\zeta(q)$ for FIRE 87 indicates a broader spectrum of increments, relative to their mean. We also note that the scaling range for the ASTEX data is

shifted compared with that of the FIRE 87 data: $\eta \approx 60$ m to $R \approx 60$ km. The factor of 3 between the FIRE 87 and ASTEX scaling ranges, the size of the structures in the respective Sc layers, coincides roughly with the ratio of boundary layer depths during the two experiments.

3. Singular measures for absolute small-scale LWC gradients

In section 2 we characterized the nonstationarity multifractal structure of marine Sc with the help of structure

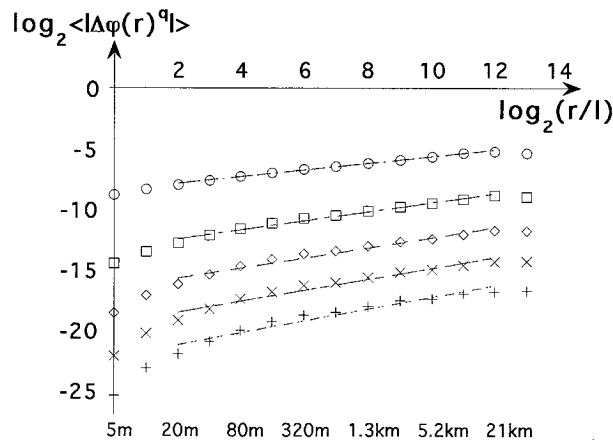


FIG. 5. Ensemble-averaged structure functions for FIRE 87 data. Structure functions $\langle |\Delta\varphi(r)|^q \rangle$, $q = 1(1)5$, vs r/l on a log-log plot for the average over all five flights from FIRE. Notice the good scaling from 20 m to 20 km, all q 's considered.

functions. It would be interesting to remove this nonstationarity from the LWC data in order to analyze the statistical properties of the remaining stationary field.

An expedient way of obtaining a stationary field from a nonstationary one with stationary increments ($1 < \beta < 3$) is to take derivatives ($\beta \rightarrow \beta - 2$). In moderately nonstationary cases such as ours with $H_1 \approx 0.2-0.4$ and $\beta \approx 1.2-1.7 < 2$, this leads to irregular gradient fields with $\beta < 0$. Alternatives include fractional differentiation, which is a power law filtering in Fourier space with an exponent greater than zero but less than one (Schmitt et al. 1992). However, this complication does not make a difference with respect to first- or even second-order derivatives in the outcome of singularity analysis (Lavallée et al. 1993; Tessier et al. 1993).

Currently, a large amount of turbulence research is focused on the role of intermittency. Multiplicative cascades are now widely accepted as models for intermittent dissipation fields in turbulent flows. We briefly discussed these models in Part I and the appendix. These models are characterized by spikiness and nonnegativity. This last feature suggests that we look at the absolute values of the gradients, taken at the smallest scale still in the scaling regime of the structure functions and/or energy spectrum; in turbulence studies, squares of velocity gradients are considered (Meneveau and Sreenivasan 1987a). For the samples of nonstationary LWC $\varphi(x)$, we have illustrated nonnegative stationary fields $\epsilon_\varphi(x)$ in Figs. 1a-e. We note the intermittent but tightly correlated episodes with spikes of different widths and heights.

Our last question is what to do with these spiky $\epsilon_\varphi(x)$ fields. Generally speaking, we wish to characterize their singularity properties. Singularity analysis comes in several variants, some of which bear multiple names in the literature: $\tau(q)$ analysis (Meneveau and Sreenivasan 1987a), trace moments (Schertzer and Lovejoy 1987), canonical measures (Chhabra et al. 1989), $f(\alpha)$ analysis

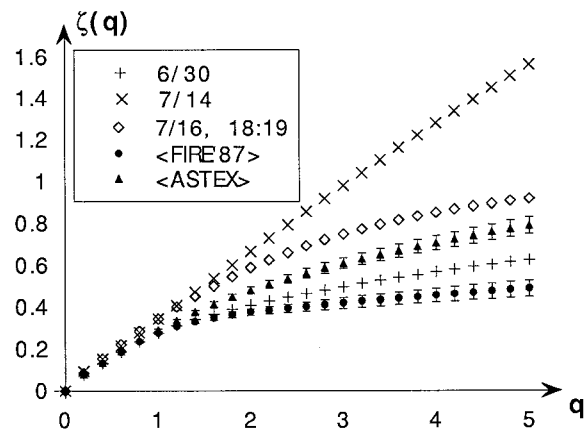


FIG. 6. Exponent function $\zeta(q)$ for LWC during FIRE 87 and ASTEX. Plain symbols: $\zeta(q)$, $q = 0(0.2)5$, for three representative datasets with different ranges of scaling: from 20 m to 5 km for 30 June (cf. Fig. 4a); from 20 m to 20 km for 1819 UTC 16 July, (Fig. 4d); from 5 m to 10 km for 14 July, without conspicuous dip (Fig. 3b). Bold symbols: $\zeta(q)$ for the average over all the FIRE 87 data and comparable ASTEX results reproduced from Davis et al. (1994a). Comparing $\zeta(5)$ for 14 July, 30 June, and the FIRE 87 average, this last one is the smallest because of the contribution of 2 July dataset (not illustrated here), the roughest of all five. The exponents and the associated error bars (for averages only) were estimated using least squares.

(Meneveau and Sreenivasan 1989), probability distribution multiple scaling (Lavallée et al. 1991), etc. We will use the simplest form and refer to it as “singular measures.”

a. Generalities and practicalities of singular measures

Given a nonstationary random atmospheric process $\varphi(x)$, $0 \leq x \leq L$ with stationary increments that is scale invariant from some outer scale R down to some inner scale η , we take the absolute value or square the gradient field at that last scale, namely, $|\Delta\varphi(\eta; x)|^m$ in the notations of the previous section with $m = 1, 2$. The scales R and η are physical quantities, independent of the instrumentally determined scales L (the total length) and ℓ (the sampling step). Recall that for the energy spectrum (Part I) scaling prevails down to the inverse Nyquist frequency ($2\ell = 10$ m), and for structure functions (section 2), we have scaling down to $\eta = 4\ell = 20$ m.

Defining $\epsilon(\eta; x)$ as a nonnegative measure of the η -scale gradient field, normalized by its mean,

$$\epsilon(\eta; x) = \frac{|\Delta\varphi(\eta; x)|^m}{\langle |\Delta\varphi(\eta; x)|^m \rangle}, \quad 0 \leq x < L - \eta, \quad (8a)$$

for either $m = 1$ (our choice, for simplicity) or $m = 2$ (as in turbulence studies); the two options can and will be compared after the analysis. Equation (8a) shows how the data $\varphi(x)$ enters the singular measures approach; in the following, we will focus on spatially degraded or coarse-grained versions of the above field. We will pa-

parameterize these by the scale r ($\eta < r \leq L$) over which the spatial averaging is performed:

$$\epsilon(r; x) = \frac{1}{r} \int_x^{x+r} \epsilon(\eta; x') dx', \quad \eta \leq x \leq L - r. \tag{8b}$$

The quantities $\epsilon(r; x)$ are referred to as measures because they are nonnegative and defined only by integrals over ‘‘boxes.’’ The basic postulate of mathematical measure theory is therefore verified: the measure associated with the union of two disjoint sets is the sum of the measures for each set.

Based on small-scale increments of $\varphi(x)$, these $\epsilon(r; x)$ fields are presumably stationary and their statistical properties are independent of x . This opens the possibility of using spatial averaging again, this time over x in Eq. (8b), in order to estimate the statistical properties of $\epsilon(r; x)$. The simplest properties of $\epsilon(r; x)$ are their one-point moments $\langle \epsilon(r; x)^q \rangle \equiv \langle \epsilon(r)^q \rangle$. We will seek the exponent $K(q)$ in

$$\langle \epsilon(r)^q \rangle \propto r^{-K(q)}, \quad q \geq 0, \tag{9}$$

adopting the notation of Schertzer and Lovejoy (1987). The condition on q in Eq. (9) is required only when vanishing $\epsilon(\eta; x)$ s occur in the data; other restrictions can apply (Mandelbrot 1974; Kahane and Periy re 1976; Schertzer and Lovejoy 1987, 1992; Gupta and Waymire 1993).

Some general results follow directly from Eq. (9). First, normalization of the pdf for $\epsilon(r; x)$ implies $K(0) = 0$; furthermore, using Eq. (8a) we find $\langle \epsilon(r) \rangle \equiv 1$ hence $K(1) = 0$. Analogous with $-\zeta(q)$ in Eq. (4), $K(q)$ will be a convex function. Since $K(0) = K(1) = 0$, convexity requires $K(q) \leq 0$ for $0 < q < 1$ and $K(q) \geq 0$ elsewhere; we will also have $K'(1) \geq 0$, a fact we will soon exploit. As for structure functions, a hierarchy of exponents can be defined, this time nondecreasing: $C(q) = K(q)/(q - 1)$, which is related to the well-known nonincreasing hierarchy of ‘‘generalized dimensions,’’

$$D(q) = 1 - C(q) = 1 - \frac{K(q)}{q - 1}, \tag{10}$$

first introduced by Grassberger (1983) and Hentchel and Procaccia (1983) with dynamical systems and strange attractors in mind. If $D(q) \equiv \text{const}$, we are dealing with a monoscaling (or ‘‘uniform’’) measure; otherwise, we talk about multiscaling (or ‘‘multifractal’’) measures. Examples of both types are presented in the appendix.

As for increments and structure functions, it is important to know what to expect for weakly variable $\epsilon(r; x)$ fields. In this case, we can anticipate $\langle \epsilon(r)^q \rangle \approx \langle \epsilon(r) \rangle^q$ (i.e., the mean can be used to estimate all other moments); Eqs. (9)–(10) then yield $K(q) = qK(1) \equiv 0$, thus $D(q) \equiv 1$, which is a ‘‘trivial’’ form of monoscaling. Otherwise, $D(q) < 1$ for $q > 0$, we are dealing with highly singular (hence skewed) ϵ distributions where, at the smallest scales, the most frequent ϵ values are

very small but now and then intense spikes occur. This is why we talk about singular measures.

We need the whole family of exponents in either (9) or (10) to characterize the intermittency in LWC, but it is convenient to define an intermittency index. Since $K(0) = K(1) = 0$, there is no linear trend in $K(q)$ such as we found for $\zeta(q)$ and parameterized with $\zeta(1)$. It is still desirable to dwell on the case $q = 1$, being one of the least affected by sampling problems. In congruence with our use of $H_1 = \zeta(1)$ for nonstationarity, we use

$$0 \leq C_1 = 1 - D(1) = C(1) = K'(1) \leq 1 \tag{11}$$

as a first-order intermittency parameter. When $C_1 > 0$, we have $D(1) < 1$; this ‘‘information dimension’’ is the fractal dimension of the sparse set where the ϵ that contribute most significantly to their (unit) mean are concentrated, thus making C_1 the information codimension. In the appendix we illustrate graphically the ideas of concentration, sparseness, and fractality, conveyed with C_1 .

b. Test case, continued

Before applying the above recipes to the LWC datasets, we will have a last look at the test data concocted in section 2b for tutorial purposes from a small portion of the 14 July run. In Fig. 7a, we have taken $\eta = \ell = 1$ for simplicity and plotted the $\epsilon(1; x) = |\Delta\varphi(1; x)|$ field derived from $\varphi(x)$ in Fig. 2a. This dataset is clearly singular ($\max_x \epsilon(1; x) / \langle \epsilon(1) \rangle \approx 63$) and correspondingly intermittent. This field is stationary since its spectral exponent is $\beta_\epsilon \approx 0.6$.

Figure 7b shows $\langle \epsilon(r)^q \rangle$ versus r for integer $q = 1, \dots, 5$ on a double log plot. The scaling is remarkably good, except for the largest r and q . Having only one sample, the large-scale values of $\langle \epsilon(r)^q \rangle$ are based on a small number of boxes, and experimentation shows that they depend highly on the precise location of the peaks. This artificial sensitivity can be tamed by using a redundant sampling of x in Eq. (8b) instead of disjoint boxes when computing the averages.

It follows from our definitions that $\langle \epsilon(r) \rangle = 1$ for all scales r , and that $\langle \epsilon(L)^q \rangle = 1$ for all q at the largest scale ($r = L$). Linear regressions were used to obtain the exponents $-K(q)$ leading to a nonnegligible intermittency parameter, $C_1 \approx 0.2$. Since the regression lines in Fig. 7b have a common intercept on the horizontal axis, their intercepts with the vertical axis are approximately proportional to $K(q)$. Now, for higher values of q , the intercepts are equally spaced, indicating that we are in a regime where $K(q)$ is quasi-linear in q . This is to be expected when sampling problems occur. Indeed, for q sufficiently large, the estimator of $\langle \epsilon(r)^q \rangle$ becomes dominated by a single intense event, $\max_x \epsilon(1; x)$. We therefore have $\max_x \epsilon(r; x) \approx \max_x \epsilon(1; x)/r$, hence $\langle \epsilon(r)^q \rangle \approx r[\max_x \epsilon(1; x)/r]^q$, that is, $\langle \epsilon(r)^q \rangle \propto r^{1-q}$ and $K(q) \approx q - 1$ for $q \rightarrow \infty$.

We will observe the onset of this linear behavior in

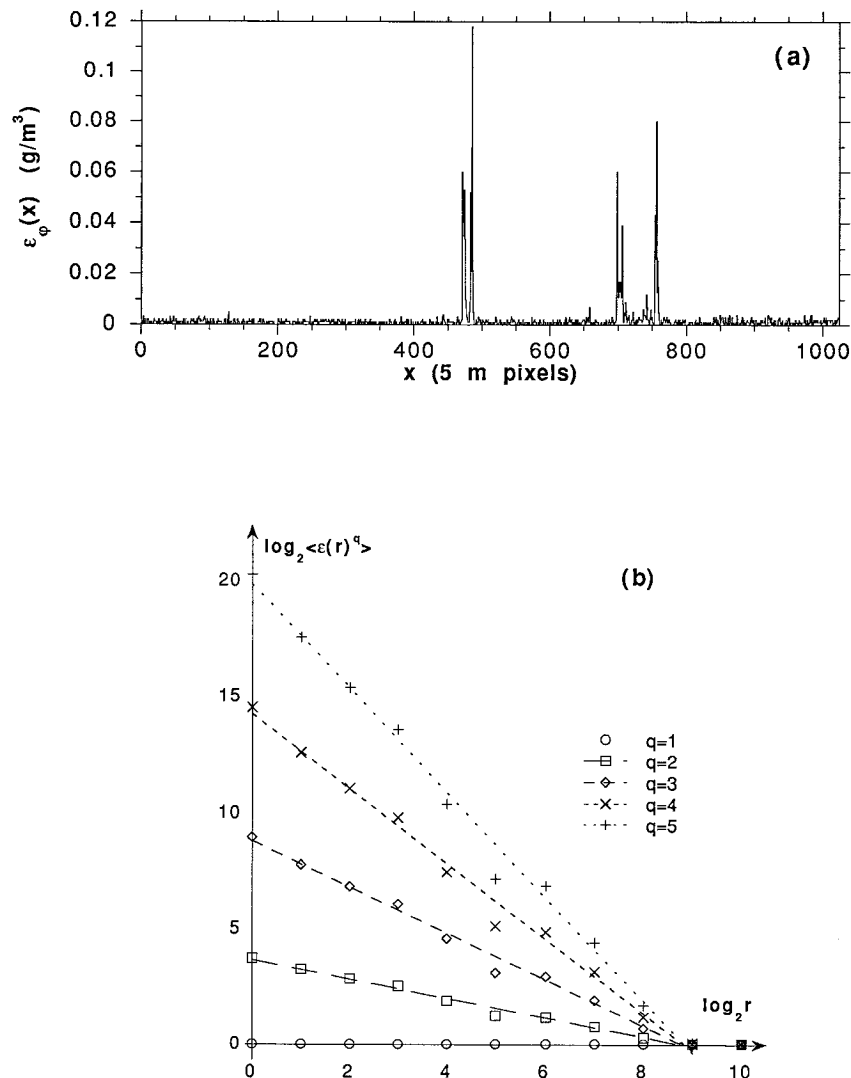


FIG. 7. Test data and singularity analysis. (a) Absolute gradient field $\epsilon(1; x) \propto |\varphi(x+1) - \varphi(x)|$ derived from the tutorial dataset in Fig. 2a for feeding the approach based on singular measures. (b) Same as Fig. 2b but for the averaged singular measures $\langle \epsilon(r)^q \rangle$, $\log_2 r = 0(1)9$ with $\ell = 1$ and $q = 1(1)5$. The multiscaling observed for $r \leq 2^8$ is traceable to the artificial features in $\varphi(x)$.

$K(q)$ for LWC in section 3c. This tells us that high enough q values have been considered. This asymptotic behavior in exponent space, $D(q) \rightarrow \text{constant}$ for $q \rightarrow \infty$, is the counterpart for singular measures of the structure function's saturation (flattening) due to poor sampling and/or violations of ergodicity observed for the structure functions with respect to scale, prior to defining exponents.

Finally, were it not for the two glitches in the test data, the outcome would have been $C_1 \approx 0$. Recall that we introduced one of the two dips artificially and that the other is probably not related to natural LWC fluctuations either. This means that singularity analysis can easily lead to wrong conclusions about the prevailing intermittency since we are not always forewarned by breaks in the scaling as is the case with q th-order struc-

ture functions. Since important structural information is lost when generating the absolute gradient field, the use of singular measures alone, without careful scrutiny of the raw data, is not recommended, especially when a single dataset is involved.

c. Results for LWC in marine Sc for FIRE 87

Figures 1a'–e' show the absolute small-scale gradient fields for the representative samples of our LWC data from FIRE 87. Figure 8 illustrates $\langle \epsilon(r)^q \rangle$ ($q = 1, \dots, 5$) for three of these datasets: (a) 30 June in Figs. 1a,a', one of the two cases deemed spiky or intermittent; (b) 14 July in Figs. 1c,c', the smooth case (with an anomalous dip); and (c) 1819 UTC 16 July in Figs. 1e,e', one of the two intermediate cases. The scale parameter

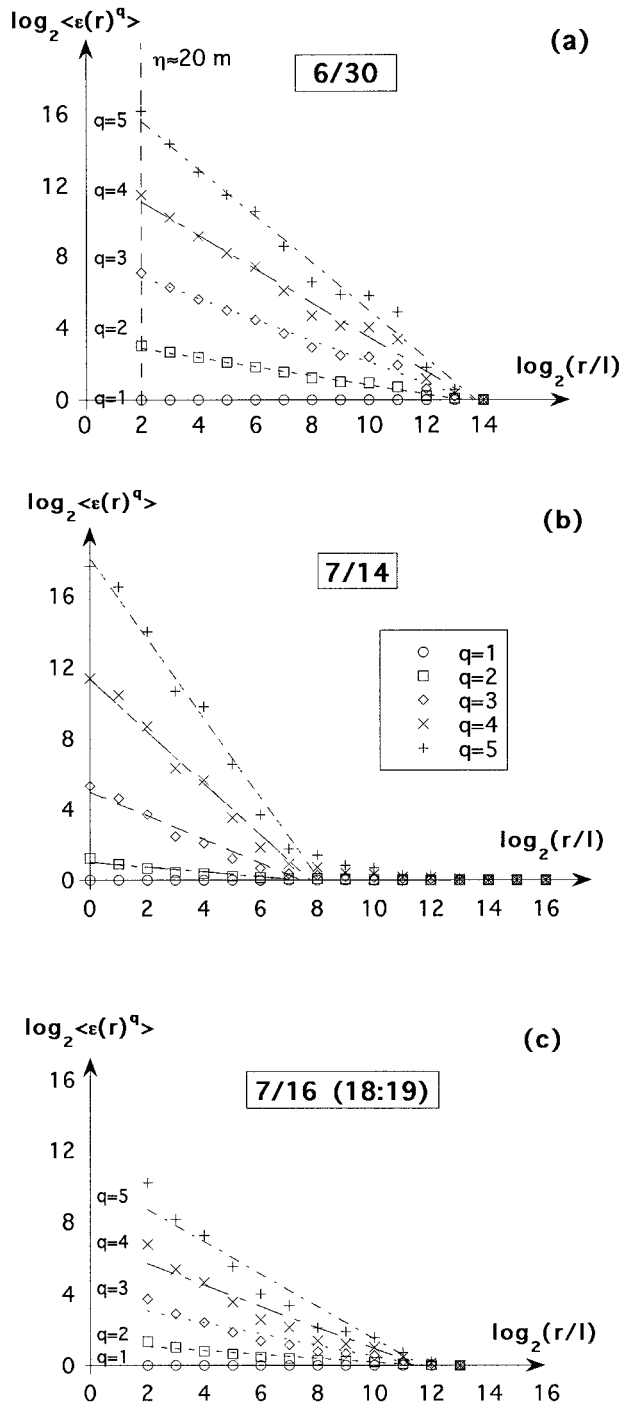


FIG. 8. Singular measures for various LWC datasets from FIRE 87. (a) $\text{Log}_2\langle\epsilon(r)^q\rangle$ for $q = 1(1)5$, vs $\text{log}_2(r/\ell)$, $4 \leq r/\ell \leq L/\ell = 2^{14}$ for the “spiky” 30 June data. See Fig. 1a for the LWC time series, denoted $\varphi(x)$; here we take $\epsilon(\eta; x) = |\Delta\varphi(\eta; x)|$, not unlike Fig. 1a’ but for $\eta/\ell = 4$ pixels rather than in $\eta/\ell = 1$. (b) Same as in (a) except for the “smooth” 14 July data (Figs. 1c,c’) and using $\eta = \ell$. (c) Same as in (a) but for one of the “intermediate” 16 July datasets (1819 UTC, Figs. 1e,e’). The multiscaling ($\langle\epsilon(r)^q\rangle \gg 1$ for $r \ll L$ and $q > 1$) behavior observed for $r/\ell < 2^7$ in (b) is traceable to the presence of an anomaly in the 14 July data (the dip $\approx 2^6$ pixels wide that is possibly artificial); the quasi-trivial ($\langle\epsilon(r)^q\rangle \approx 1$) behavior obtained for $r/\ell \geq 2^7$ is probably more representative of this flight. In (a) and (c) there is no break in the scaling and the multiscaling is not believed to be spurious.

r goes from $\eta = 4\ell = 20$ m to $L = 2^{14}\ell \approx 82$ km (for 30 June) and to $L = 2^{13}\ell \approx 41$ km (for 16 July); finally, for 14 July, it goes from $\eta = \ell = 5$ m to $L = 2^{16}\ell \approx 330$ km.

Figure 1a’ (30 June) is reminiscent of a reasonably intermittent multifractal cascade model; thus, the corresponding $\text{log}_2\langle\epsilon(r)^q\rangle$ s are linear in $\text{log}_2 r$ over the full range of scales (from $\eta = 20$ m to $L = 84$ km). The absolute slopes defining the $K(q)$ exponents are displayed in Fig. 10 and are sampled more frequently. We notice the anticipated convexity and the predetermined values $K(0) = K(1) = 0$. The important C_1 parameter is computed by numerical differentiation of $K(q)$ at $q = 1$, yielding 0.14.

In contrast, Fig. 1c’ (14 July) is unlike a cascade process: the two spikes are as anomalous as the dip in Fig. 1c, marking its beginning and end. For scales larger than the dip ($8 \leq \text{log}_2(r/\ell) \leq 15$), the singular measures are characteristic of homogeneity (roughly constant $\langle\epsilon(r)^q\rangle$). For smaller scales, the probably spurious spikes induce an intense multiscaling. Avoidance of the dip reduces the range of scales but almost completely eliminates the multiscaling. The scaling is not illustrated, but the new slopes are plotted in Fig. 10 and the associated C_1 is very small, ≈ 0.03 . This is “residual” or “spurious” multifractality, namely a multiscaling associated with weak variability but entirely traceable to the finite amount of data (hence range of scales) involved. Spurious multiscaling is discussed for specific models by Aurell et al. (1992), Marshak et al. (1994), Eneva (1994), and in general terms by Davis et al. (1996b).

The singularity properties of the data in Fig. 1e’ (1819 UTC 16 July) are illustrated in Fig. 8c. The quality of the scaling is degraded but, as expected, the degree of multiplicity (range of slopes) is intermediate between the first case (30 June) and the second case (14 July) without the presumably artificial glitch in the data. The exponents obtained for $2 \leq \text{log}_2(r/\ell) \leq 11$ are plotted in Fig. 10. Unsurprisingly, C_1 is also intermediate ≈ 0.07 . Note that in all three cases above, the $K(q)$ curves in Fig. 10 become straight for the largest q due to the dominance of a single event, as explained in section 3b for the test data.

d. Comparison of average singularity properties for FIRE 87 and ASTEX

In Fig. 9, $\langle\epsilon(r)^q\rangle$, cumulated over all five FIRE 87 datasets, shows good scaling over the full range of available scales: $2 \leq \text{log}_2(r/\ell) \leq 13$. As for structure functions, we do not go further in order to have at least one contribution per dataset to the average. The corresponding exponents are carried over to Fig. 10. The most intermittent datasets (30 June and 2 July) dominate the average for large q . For small q , the $K(q)$ obtained by averaging $\langle\epsilon(r)^q\rangle$ over all five datasets is closer to those

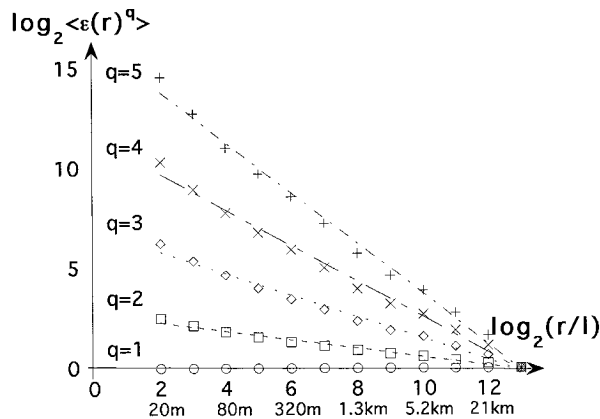


FIG. 9. Ensemble-averaged singular measures for FIRE 87 data. Same as Fig. 8 except for the average of all five datasets. No break of scaling is observed from 20 m to 40 km.

of the intermediate datasets. We find $C_1 \approx 0.10$ for the ensemble average.

We have reproduced in Fig. 10 Davis et al.'s (1994a) results for $K(q)$ obtained from LWC fluctuations inside marine Sc during ASTEX. The agreement with the FIRE 87 data is good for small values of q , those associated with the well-sampled values of $\epsilon(r; x)$; for instance, $C_1 \approx 0.08$ for ASTEX. At any rate, the large ranges of scales and of associated $K(q)$ confirm the multifractal nature of marine Sc, this time in connection with the singularity properties of LWC's absolute gradients. Also confirmed is the first-order independence with respect to the local climatology of the nonlinear dynamics governing the structure of these clouds, this time in connection with their intermittency properties.

4. Utility of multifractal analyses

a. Removing spectral ambiguity

In Part I we used spectral analysis to study LWC in marine Sc but also reassessed its utility at large, beyond being the standard procedure for characterizing spatial correlations in data. We found that $E(k)$ is a rather poor discriminator between different models and/or datasets but also that, in conjunction with scale invariance, it has the power to separate two broad classes of process: stationary, or nonstationary. This is extremely useful since the two categories call for different treatments in physical space statistics. For instance, running means are, at best, difficult to interpret in nonstationary regimes; it is better to focus on spatial averages using increments.

In sections 2 and 3, we have proposed multifractal analysis in physical space as a means to overcome the fundamental ambiguity of a purely spectral approach. In the remainder of this section, we go beyond this necessary exercise and address the same question as for $E(k)$ and β : what is the real utility of structure functions

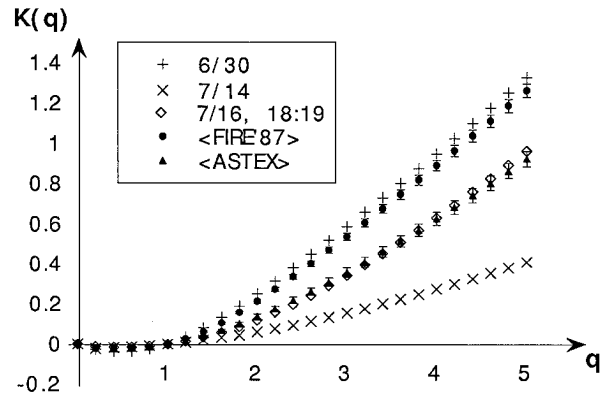


FIG. 10. Exponent function $K(q)$ for LWC during FIRE 87 and ASTEX. Plain symbols: $K(q)$, $q = 0(0.2)5$, for the three datasets used in Fig. 8; for 14 July, however, the suspicious dip was avoided and the new $K(q)$ are all much smaller. Bold symbols: $K(q)$ for the overall average of the FIRE 87 data (using the results in Fig. 9 from 20 m to 40 km) and comparable ASTEX data.

and $\zeta(q)$, singular measures and $K(q)$? The answer is first registered in some carefully selected examples and then stated in general words.

b. Quantifying/qualifying nonstationarity with structure functions

In Part I, stationary behavior was mapped to $\beta < 1$ for scale-invariant processes and, from Eq. (5), we see that in the stationary limit $\beta \rightarrow 1^+$ as $\zeta(2) \rightarrow 0^+$, implying $\zeta(q) \equiv 0$ because of its analytical properties listed in section 2a. This reflects the fact that stationarity per se (all statistical properties are invariant under translation) implies stationary increments. However, barring finite-size effects (Davis et al. 1996b), increments have trivial statistics, that is, $\zeta(q) \equiv 0$ in Eq. (4), since invariance by translation over arbitrary distances implies statistically scale-independent increments.

So nontrivial structure functions imply a degree of nonstationarity. Can we actually measure nonstationarity? Is it not an "on-off" attribute? This is indeed possible as soon as we have a well-defined scale-invariant regime, not a strong constraint for LWC or other atmospheric data. The complete $\zeta(q)$ or $H(q)$ is clearly required to describe the data's nonstationarity in general. However, we only need a single exponent to quantify the amount of nonstationarity. We have singled out H_1 for this purpose, essentially for historical reasons but its robustness with respect to glitches, as demonstrated in section 2b, is welcome. With this *quantification* in mind, we can perceive the remainder of the exponent as a means to *qualify* the nonstationarity. Consider the following examples.

- *Different amounts of monoscaling nonstationarity.* Figure 11 shows a progression of increasingly nonstationary processes. The upper case is a sample of $1/f$ noise that is marginally stationary according to our

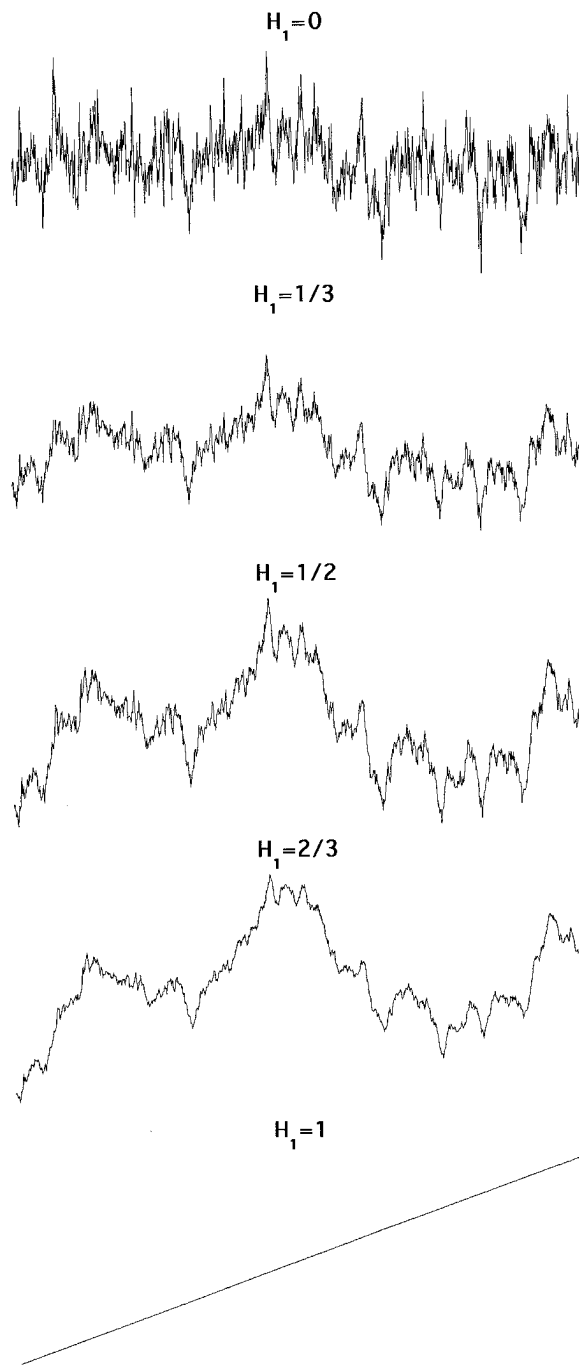


FIG. 11. Different amounts of the same kind of nonstationarity. Samples of fBm $\varphi(x)$ on the interval $0 \leq x \leq L = 1024$, for $H_1 = 0, 1/3, 1/2, 2/3$ and 1 , from top to bottom. The nonstationarity parameter H_1 increases from the marginally stationary case ($1/f$ or flicker noise at $H_1 = 0$) to the extreme case of a noiseless linear trend ($\varphi(x) = x/L$). This one-parameter ($0 \leq H_1 \leq 1$) family of processes are all nonstationary ($\beta = 2H_1 + 1 > 1$) with stationary increments ($\beta < 3$) and can be said to have the same kind of nonstationarity, namely, the monoscaling kind: $\zeta(q) = qH_1$ or $H(q) \equiv H_1$.

spectral criterion ($\beta = 1$); it has $H(q) \equiv 0$, and $H_1 = 0$ in particular. The middle case is Brownian motion (Bm), the prototypical nonstationary signal that has $H(q) \equiv H_1 = 1/2$ (hence $\beta = 2$). The lower case is a noiseless linear trend ($H_1 = 1$) representative of differentiable functions ($\beta \geq 3$). The two remaining cases are samples of Mandelbrot's (1977) fractional Brownian motion (fBm) equally distant from Bm on the nonstationarity scale defined by H_1 : respectively, $H_1 = 1/3$ (the more stationary and rough) and $H_1 = 2/3$ (the less stationary and more smooth). A characterizing property of fBm is its monoscaling, namely, $H(q) \equiv H_1$. So all the examples in Fig. 11 differ in the amount of nonstationarity present (as measured by H_1), but they all have the same kind of nonstationarity in the sense that no other parameter than H_1 is needed to describe it; more precisely, they are all of the monoscaling type.

- *Qualitatively different but equally extreme cases of nonstationarity.* We can conjure up two situations of extreme nonstationary behavior. First consider $\varphi(x) = ax + b$ (as in Fig. 11, bottom case) where a and b are random. The definitions in (6)–(7) lead to $\langle |\Delta\varphi(r)|^q \rangle = \langle |a|^q r^q \rangle$, hence $\zeta(q) = q$ and $H(q) \equiv 1$ for any q . Now take $\varphi(x) = aL\Theta(x - c) + b$ where $\Theta(\cdot)$ is the Heaviside step function and c is uniformly distributed on $[0, L]$; a and b are unchanged, so $\varphi(0)$ and $\varphi(L)$ are the same as in the previous example. The probability of c falling in any segment of length r is r/L ; in this case the increment is aL , otherwise is null. So this model yields $\langle |\Delta\varphi(r)|^q \rangle = \langle |a|^q \rangle L^q \times (r/L) + 0 \times [1 - (r/L)]$ for $0 < r \leq L$, hence $\zeta(q) \equiv 1$ and $H(q) = 1/q$ for $q > 0$. The structure functions tell us that these two models may both be of extreme nonstationarity (the same $H_1 = 1$ arises) but, as expected, they differ qualitatively (different $H(q)$ s for $q \neq 1$).
- *Qualitatively different cases of moderate nonstationarity.* In Part I, we used Cahalan et al.'s (1994a) fractal cloud models based on bounded cascades to illustrate nonstationarity; Marshak et al. (1994) showed these models to be multiscaling with $H(q) = \min\{H, 1/q\}$, $H \geq 0$ being a free parameter, hence $H_1 = \min\{H, 1\}$. Bounded cascades are therefore statistically distinguishable, in the sense of structure functions, from fBm (with the same $H_1 = H < 1$), provided moments of order $q > 1/H$ are considered.

c. Quantifying/qualifying intermittency with singular measures

Unlike stationarity, intermittency is a rather fuzzy concept a priori. Nevertheless, it plays the same role for singular measures as nonstationarity does for structure functions. In this case, the *quantifier* of intermittency is C_1 ; indeed, $C_1 = 0$ implies $K(q) \equiv 0$ (no intermittency whatsoever) because of its analytical properties listed in section 3a. The remainder of $K(q)$ or $D(q)$, $q \neq 1$, is

needed to *qualify* the intermittency. The following examples clarify this statement.

- *Similar multiscaling with different C_1 .* Figure 12 shows a progression of more and more intermittent processes from top to bottom using multiplicative cascade models $\epsilon(x) = \prod_i W_i$ with random weights $W > 0$ such that $\langle W \rangle = 1$. These processes have multiscaling singular measures: $K(q) = \log_2 \langle W^q \rangle$ for q such that $\langle \epsilon(r)^q \rangle < \infty$; thus, $C_1 = \langle W \log_2 W \rangle \geq 0$ where “=” corresponds to flat fields ($W = 1$, with no dispersion) from Eq. (11). If $C_1 > 0$, these models are referred to as multifractals and indeed their different level or exceedance sets have different fractal dimensions (cf. the appendix). In this case, we took log-normally distributed W that give $D(q) = 1 - C_1 q$ (Kolmogorov 1962; Monin and Yaglom 1975) for $q < 1/C_1$ (Mandelbrot 1974; Schertzer and Lovejoy 1987). Thus we have a sequence of qualitatively similar models with an increasing amount of intermittency (as measured by C_1).
- *Monoscaling intermittency models, different C_1 .* A dramatic example of intermittency is given by randomly positioned Dirac δ functions (actually measures): $\epsilon(x) = L\delta(x - c)$ where c is uniformly distributed on $[0, L]$. In this theoretical model, integrals of $\epsilon(x)$ over $[x, x + r]$ yield either 0 or L , depending on whether c is between the bounds (probability r/L) or not. Taking the q th power, then averaging both sides of Eq. (8b), yields $\langle \epsilon(r)^q \rangle = [L/r]^q \times (r/L) + 0^q \times [1 - (r/L)]$, hence $\langle \epsilon(r)^q \rangle \propto r^{1-q}$ for $q > 0$. Identifying with Eq. (9), we obtain $K(q) = q - 1$, thus $D(q) \equiv 0$ and $C_1 = 1$ from Eqs. (10)–(11). Another example of intermittency is the famous “middle-third” Cantor set and its associated measure discussed in the appendix; with its $D(q) \equiv 1 - C_1$ where $C_1 = \log_2 / \log_3 < 1$, it has the same (monoscaling) type of intermittency as the Dirac measure but in a lesser amount (as measured by C_1).
- *Different kinds of multiscaling, same C_1 .* In the appendix we illustrate intermittency with the log-binomial p model (Meneveau and Screenivasan 1987b). Like the lognormal models in Fig. 12, these are generated with a multiplicative cascade. However, their $D(q)$ hierarchy is very different from that of the lognormal model, reflecting the fact that the p model’s multiplicative weights obey a discrete Bernoulli law. Nonetheless, by varying the log-binomial model’s free parameter p in $[0, 1/2]$, its $C_1 = 1 + p \log_2 p + (1 - p) \log_2 (1 - p)$ can take on any value in $[0, 1]$ and match the value for a lognormal model.

d. Separating nonstationarity ($\beta > 1$) from intermittency ($C_1 > 0$)

The Gaussian notion of an “outlier,” a rare but intense event, can be mistaken for a manifestation of nonstationarity. For instance, conventional wisdom tells us

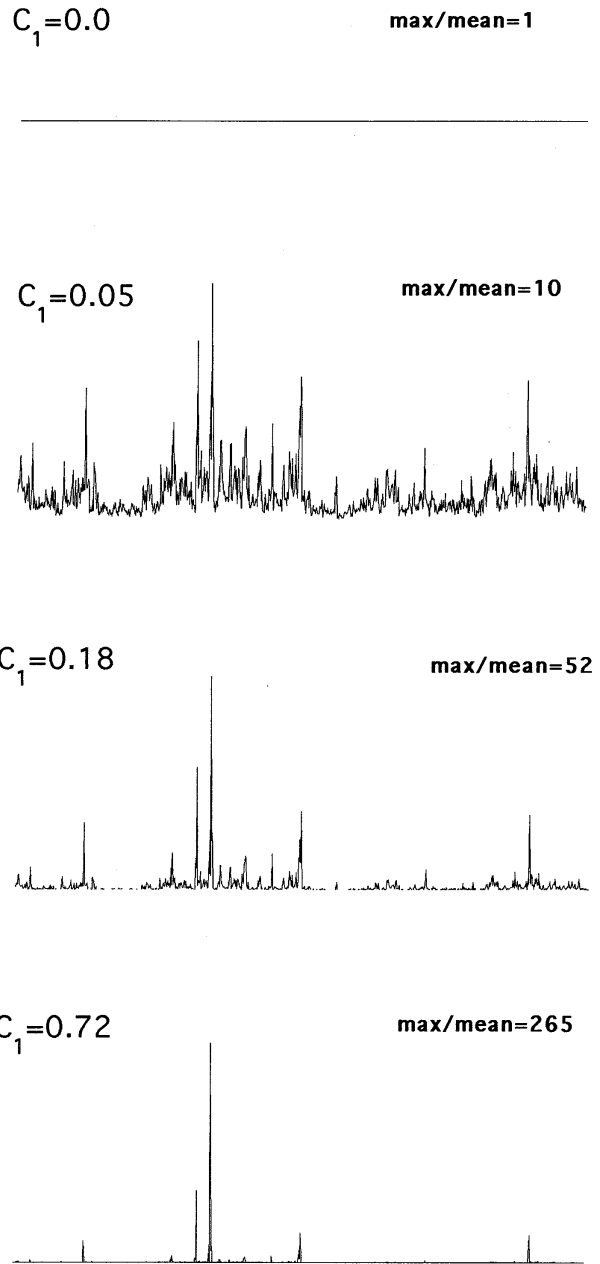


FIG. 12. Different amounts of the same kind of intermittency. Log-normal cascades $\epsilon(x)$ on the interval $0 \leq x \leq L - 1$ with $L = 1024$, for $C_1 = (\sigma_{\ln w})^2 / 2 \ln 2$ with, from bottom to top, $\sigma_{\ln w} = 0, 0.25, 0.5$, and 1. The procedure is repeated nine more times, using ever smaller intervals down to a single pixel. This one-parameter ($0 \leq C_1 \leq 1$) family of cascade processes have the same kind of intermittency, namely, log-normal: $K(q) = C_1 q(q - 1)$; hence $D(q) = 1 - C_1 q$ for $q < 1/C_1$. They are all stationary ($\beta_\epsilon = 1 - K(2) = D(2) < 1$) and the intermittency index C_1 increases as we move from the flat field case ($C_1 = 0$), via $C_1 \approx 0.045$ and $C_1 \approx 0.18$, to $C_1 \approx 0.72$. For $C_1 > 1$ ($\sigma_{\ln w} > \sqrt{2 \ln 2} = 1.177\dots$), the cascade is “degenerate”: most realizations would be essentially empty ($\epsilon(x) \approx 0$) but now and then a huge spike would occur somewhere. The theory quoted here was developed largely by Kolmogorov (1962), Obukhov (1962), Mandelbrot (1974), Kahane and Peirière (1976), and Schertzer and Lovejoy (1987, 1992).

that the random occurrence of a strong spike in the midst of low-amplitude uncorrelated fluctuations is the signature of nonstationarity, the argument being that variance in the spike perturbs significantly standard second-order statistics such as the wavenumber spectrum $E(k)$ (which ignore event localization). In contrast, we view this situation as the superposition of two stationary processes. Indeed, both have vanishing β (hence $<$ unity). However, one process is nonintermittent (the white noise), the other extremely intermittent (the δ function). The (generally tentative) Gaussian dichotomy between typical or normal events and outliers, flukes, or anomalies is absorbed naturally into the more productive multifractal framework for data analysis where intermittency, rather than nonstationarity, is the key concept.

This does not mean that intermittency and nonstationarity are always easy to separate. Actually, one can question the degree of independence of the families of exponents $\zeta(q)$ and $K(q)$. Are we not looking at the system's multifractality in two different ways? If so, how are they related? This open issue is surveyed by Davis et al. (1993, 1994b). At any rate, one new exponent at least is needed to go from singular measures and $K(q)$ to structure functions and $\zeta(q)$; let us assume this extra parameter to be H_1 . If such a one-to-one $\zeta(q) \leftrightarrow K(q)$ connection exists, then one can spell out a procedure to obtain $K(q)$ from the deviation of $\zeta(q)$ from a straight line; consequently, singular measures would become redundant.

e. Relaxing Gaussian assumptions about data

In the turbulence literature (e.g., Monin and Yaglom 1975), $K(2)$ in Eq. (9) is designated as “the” intermittency parameter, recalling that $m = 2$ is used in Eq. (8a) to derive the dissipation field from velocity. By the same token, the structure function for $q = 2$, namely, $D(r) = \langle [\varphi(x+r) - \varphi(x)]^2 \rangle$ used in Part I, is sometimes still referred to as “the” structure function. At any rate, $D(r)$ plays a central role in geostatistics where it is known as the “semi-variogram” (Christakos 1992). This emphasis on the second-order moments is a natural consequence of Gaussian thinking that variability is generally amenable to variance and covariance. This framework proves too narrow for cloud LWC variability: out of the five FIRE 87 datasets, only one (14 July) exhibits approximately Gaussian behavior.

Gaussian statistics have developed to a high level of mathematical sophistication, primarily in response to issues in psychometrics and signal processing. A new statistical paradigm is clearly required to deal properly with variability in large physical systems such as clouds, or the atmosphere as a whole. Wavelets with (Muzy et al. 1994) or without (Lau and Weng 1995) multifractal formalism seem to be fulfilling this need.

5. Marine stratocumulus in the bifractal plane

In many applications, the two continuous exponent functions $\zeta(q)$ and $K(q)$ may be too much to deal with; for instance, in stochastic modeling we like to keep the number of free parameters to a strict minimum. As a way of narrowing the possibilities, we have underscored previously the importance of the values at $q = 1$ of the monotonic exponent hierarchies $H(q)$ and $D(q)$.

a. Introducing the bifractal plane

Choosing a single exponent to represent a whole multifractal approach is not a simple matter. It even seems counterproductive until one realizes that quantifying nonstationarity with $H_1 = H(1)$ and intermittency with $C_1 = C(1)$ is already a big step in both data analysis and numerical modeling tasks. The selected coordinates (H_1, C_1) are indices of nonstationarity and intermittency: H_1 and C_1 vanish in stationarity cases and in the absence of intermittency, respectively. So H_1 measures nonstationarity and C_1 intermittency naturally, starting at zero, ending at unity. As a first-order description of structure in atmospheric data, the (H_1, C_1) plane is likely to find many applications. Here we will use it as a graphic tool to summarize our results. Figure 13 shows such a plot, and we have highlighted it with theoretical and empirical results from this paper and from the literature.

It is difficult to fully appreciate the multiscaling of an atmospheric process or model without leaving the (H_1, C_1) plane. Another approach to multifractal characterization of data with a minimal number of parameters has been devised by Schertzer and Lovejoy (1987). It is based on the concept of “universal” multifractality where an exponent α , the Lévy index, describes various kinds of intermittency and runs between 0 (monofractality) and 2 (lognormality). Lavallée et al. (1993) use “double trace moments,” a variant on singularity analysis, to obtain C_1 but their estimate is subordinated to a prior one of α . Their “nonconservation” parameter is derived from β knowing both α and C_1 .

b. Atmospheric fields and models in the bifractal plane

Five points (with error bars around the size of the dots) plotted on the multifractal plane in Fig. 13 correspond to the various LWC datasets from FIRE, illustrated in Figs. 1a–e and analyzed in sections 2 and 3. The black asterisk shows H_1 and C_1 for the average of all five flights, which are obtained from Figs. 5 and 9. The scatter of the individual spatial averages around the ensemble average illustrates ergodicity violation, a strong argument in favor of nonergodic models. This dispersion also stresses our need for vast amounts of data and this data should be collected as systematically as possible, without looking for any special type of event.

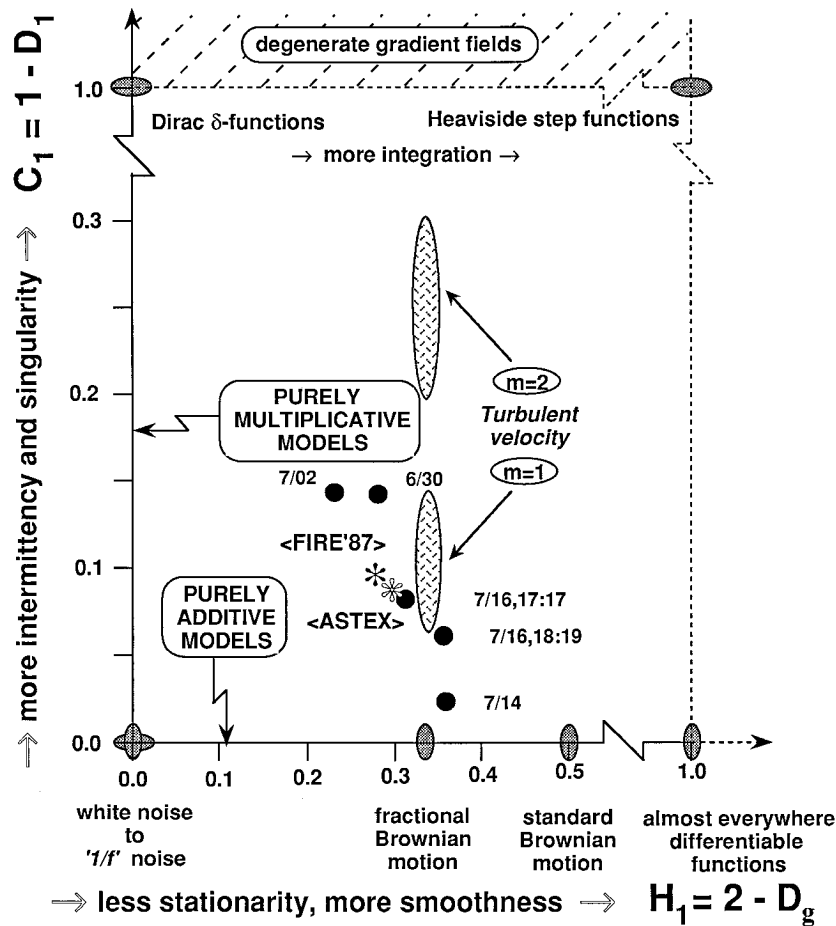


FIG. 13. Marine Sc, turbulence, and stochastic models in the bifractal plane. The index of nonstationarity H_1 increases horizontally and refers to the signal increments. The intermittency index C_1 increases vertically and refers to the absolute η -scale gradient field. In both cases the accessible range goes from zero to unity; situations where $C_1 > 1$ [note the information dimension $D(1)$ is negative] correspond to degenerate gradient fields that vanish almost everywhere in almost every realization. The horizontal and vertical axes are hosts respectively to nonstationary and nonintermittent additive models (fractional Brownian motions) in Fig. 11 and their intermittent and stationary multiplicative counterparts (turbulent cascade models) in Fig. 12. Atmospheric data lives inside the unit square and cannot be matched by either type of model. This underscores the need for new hybrid models.

Davis et al.'s (1994a) results for H_1 and C_1 from AS-TEX have been added to Fig. 13 (white asterisk). They are also based on five different flight sections, selected to be inside cloud and relatively long, as is the case for the FIRE 87 data. Their ensemble-average mean multifractal parameters, $(H_1, C_1) \approx (0.29, 0.08)$, are very close to their FIRE 87 counterparts, $\approx (0.28, 0.10)$. This remarkable proximity can be interpreted as a consequence of the common nature of the nonlinear physical processes that determine the internal structure of marine Sc. However, the scaling range involved depends on the locale, roughly in proportion with the thickness of the boundary layer (BL): 20 m–20 km off the coast of southern California (BL thickness ≈ 0.5 km) versus 60 m–60 km in the mid-Atlantic (BL thickness ≈ 1.5 km).

A clear message of the (H_1, C_1) plot in Fig. 13 is that

neither the additive- nor the multiplicative-type cascade processes, plotted, respectively, in Figs. 11 and 12, are satisfactory models for LWC fluctuations. Indeed, additive processes (fBms) are nonstationary ($0 < H_1 < 1$) but nonintermittent ($C_1 = 0$), while their multiplicative counterparts (turbulent cascades) are intermittent ($0 < C_1 < 1$) but stationary ($H_1 = 0$). These models are therefore inadequate to represent either turbulent velocity or LWC in marine Sc. There is a need for hybrid stochastic models with both additive (nonstationary) and multiplicative (intermittent) features for turbulent velocity, LWC in clouds, and probably other atmospheric fields.

We have indicated approximate locales on the (H_1, C_1) plane of turbulent velocity data. The abscissa $H_1 \approx 1/3$ reflects approximately Kolmogorov's (1941)

scaling law: $\zeta(2) = 2/3$, $\beta = 5/3$. The ordinate $C_1 \approx 0.25 \pm 0.05$ was estimated by Schmitt et al. (1992). They used the definition of $\epsilon(\eta; x)$ as $|\Delta\varphi(\eta; x)|^2$ [$m = 2$ in Eq. (8a)]. To compare it with the C_1 values of our LWC data, we find its counterpart for the measure $\epsilon(\eta; x)$ as $|\Delta\varphi(\eta; x)|$, that is, $m = 1$ in Eq. (8a). Using Lavallée et al.'s (1993) formulas for universal multifractals, one can show that $C_1^{(m=1)} = 2^{-\alpha} C_1^{(m=2)}$ where $0 \leq \alpha \leq 2$. Finally, taking into account the estimated range of parameter α for the turbulent velocity data as $\alpha = 1.3 \pm 0.1$ (Schmitt et al. 1992), we find $C_1 = C_1^{(m=1)} \approx 0.11 \pm 0.04$, not unlike the values we obtain for LWC.

Whether dynamic or stochastic, a realistic cloud model should be mapped to an (H_1, C_1) point as near as possible to the one that represents the data. This would constitute a statistically robust, simple yet comprehensive test for structural congruence that treats model output and data on an equal footing. Atmospheric field retrievals from remotely sensed imagery operate on a per pixel basis, often making invalidated homogeneity assumptions for subpixel scales for operational reasons. Retrieved fields should therefore be treated in the same way as model output and compared with in situ probings for compatibility in H_1 and C_1 ; steps in this direction are taken by Marshak et al. (1995b).

6. Conclusions

We have shown that the internal horizontal structure of marine stratocumulus (Sc) clouds during FIRE is scale invariant over a large range of scales: 20 m–20 km. By scale invariant, we mean that the two-point statistics of all orders associated with LWC can be parameterized with power laws in r , the distance between the two points of interest. The scaling range straddles the typical thickness of such clouds (≈ 300 m) as well as that of the whole boundary layer (≈ 0.5 km). Previously reported breaks of scaling (≈ 200 m) in Landsat radiance fields associated with the same FIRE 87 marine Sc (Cahalan and Snider 1989) are not observed in the LWC field, which argues for a radiation transport-based explanation.

Davis et al. (1997) study the scaling properties of numerically simulated Landsat cloud scenes and find that there is a characteristic “radiative smoothing” scale proportional to the harmonic mean of transport-mean-free path and geometrical cloud thickness (Marshak et al. 1995b). This scale measures the effect of net horizontal radiative fluxes: for scales larger than it, cloud liquid water and radiation fields fluctuate together, while for small scales, radiation fields are much smoother.

Following a well-established tradition in turbulence studies, we have complemented the spectral analysis used in Part I ($E(k) \sim k^{-\beta}$, $\beta \approx 1.4$), which is second order, with two physical space multiscaling techniques: q th-order structure functions and singular measures, both of which are explained in general terms and then

applied to LWC data. Each multifractal approach yields a whole family of exponents. The statistical nonstationarity of the LWC distribution is captured by the structure functions and its intermittency is targeted by the singular measures. Structure functions use the stationary increments of the nonstationary data, whereas singular measures use a nonnegative stationary field derived from the data by taking the absolute values of the small-scale gradients. In both cases we find nontrivial multiscaling that, given the wide range of scales involved, establishes the nonstationary multifractal nature of marine Sc.

The connection between intermittency and nonstationarity remains an open question where deviations from Gaussian behavior play a key role. Following Davis et al. (1994a), we advocate the bifractal plane to characterize these basic scale-invariant properties for any atmospheric signal recorded in time and/or space. Both coordinates are exponents: H_1 measures the nonstationarity and C_1 the intermittency, both on a scale from zero to unity. Nonstationarity and intermittency are probably the most difficult aspects of atmospheric dynamics to capture with numerical models, and we generally resort to stochastic approaches instead. Quantifying these concepts is a preliminary step toward meeting this challenge.

Having applied a comprehensive spectral–multifractal analysis to marine Sc LWC fields sampled during FIRE 87 and ASTEX, we find the two corresponding points in the (H_1, C_1) plane to be close: (0.28, 0.10) for FIRE 87 and (0.29, 0.08) for ASTEX. This is another indication that the dynamics determining the internal structure of marine Sc depend little on the local climatology; this echoes our spectral argument in Part I ($\beta_{\text{FIRE 87}} \approx \beta_{\text{ASTEX}} \approx 1.4$) for a degree of universality in the thermo–hydrodynamical processes that shape marine Sc. To first order, ASTEX Sc behave statistically like scaled-up versions of FIRE 87 Sc, in a ratio approximately equal to that of the boundary layer thicknesses. We also note that both the H_1 and C_1 for LWC are comparable to those of velocity, temperature, and admixture fluctuations in turbulence. Finally, the (H_1, C_1) plot shows that neither multiplicative cascades (with $H_1 = 0$) nor additive Gaussian models such as fractional Brownian motions (with $C_1 = 0$) adequately reproduce the LWC fluctuations in marine Sc or, for that matter, turbulent velocity signals. So there is a pressing need for a new class of hybrid stochastic cloud models that will likely find their first applications in the next round of radiation transport simulations.

Acknowledgments. This work was supported by the Environmental Sciences Division of the U.S. Department of Energy (under Grant DE-A105-90ER61069 to NASA's Goddard Space Flight Center) as part of the Atmospheric Radiation Measurement (ARM) program. We are grateful to Prof. P. Austin and Drs. M. King and T. Arnold for giving us access to the FIRE archives. We also thank A. Arnéodo, B. Baker, M. Baker, J.-L. Bren-

guier, C. Duroure, H. Gerber, H. Isaka, D. Lavallée, S. Lovejoy, C. Meneveau, R. Pincus, D. Schertzer, F. Schmitt, Y. Tessier, and T. Warn for fruitful discussions.

APPENDIX

Geometrical Interpretations of Multifractal Properties

In this appendix, we survey the geometrical interpretation of both singular measures and structure functions, thus justifying usage of the terms “fractal” and “multifractal.”

a. From fractal sets to mono- and multifractal measures

Let $N(r)$ be the number of r -sized boxes needed to cover some subset S of d -dimensional Euclidean space, $d = 1, 2, 3$. Then consider the simplest way of covering S : count the number $N(r)$ of cells of a d -dimensional grid of constant r that intersect S . The set’s fractal dimension $D_f(S)$ is then defined by

$$N(r) \sim r^{-D_f(S)}, \tag{A1}$$

where “ \sim ” means we are disregarding proportionality constants and slowly varying terms such as powers of $\log r$.

A deterministic monoscaling example: The prototypical fractal known as Cantor’s “middle-third” set (denoted C in the following) is illustrated in Fig. A1; its simple construction leads to $D_f(C) = \log_{1/r} N(r) = \log_3 2 = 0.631 \dots$ from Eq. (A1). A measure $\epsilon_C(x)$ can be associated with this sparse subset of $[0, 1]$ using the following cascade procedure. Start with $\epsilon_C(x) \equiv 1, 0 \leq x \leq 1$ and recursively multiply it by zero in the middle third of every threefold subdivision. In the first and last thirds, $\epsilon_C(x)$ is multiplied by $3/2$, thus maintaining the spatial average of $\epsilon_C(x)$ at unity for all stages of the construction. Other moments of $\epsilon_C(x)$ are easily computed. After n steps there are 3^n intervals and the scale of interest is $r = r_n = 1/3^n$, however, only $N(r_n) = 2^n$ of these cells are still “alive” and each one carries a value $\epsilon_C(r_n; x) = (3/2)^n$; all the others are “dead” with $\epsilon_C(r_n; x) = 0$. So we have

$$\begin{aligned} \langle \epsilon_C(r_n)^q \rangle &= [(3/2)^n]^q \times (2/3)^n + 0^q \times [1 - (2/3)^n] \\ &= (1/3^n)^{(q-1)\log_{1/3}(3/2)}, \quad q > 0. \end{aligned} \tag{A2}$$

Identifying with $r_n^{-K(q)}$, we find $K_C(q) = [1 - \log_3 2](q - 1)$, hence $C_C(q) = K_C(q)/(q - 1) \equiv 1 - \log_3 2$, and

$$D_C(q) \equiv \log_3 2, \quad q > 0. \tag{A3}$$

This is a case of monoscaling, since a single exponent defines all the “statistical” properties of this model; in particular, we retrieve the fractal dimension $D_f(C) = \log_3 2$ of the Cantor set from any $D_C(q)$. The constancy of $D_C(q)$ reflects the fact that the measure $\epsilon_C(x)$ is uniformly distributed over its support.

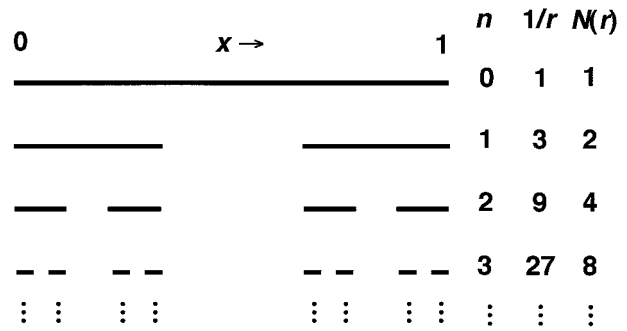


FIG. A1. Construction of Cantor’s “middle-third” fractal set with $D_f = \log_3 2 \approx 0.63$.

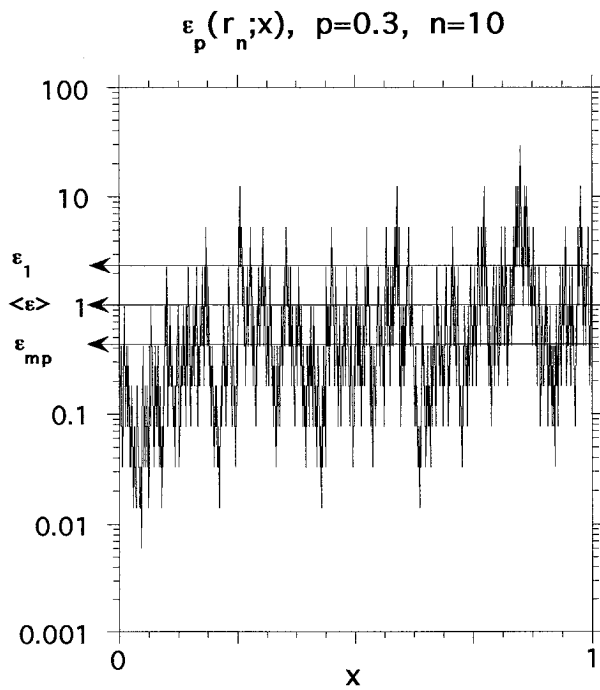
A stochastic monoscaling example: Randomly positioned δ functions can be generated by a similar cascading procedure: divide intervals in 2 rather than 3 and multiply right and left, or vice versa (with equal probability), by 0 and 2. The same calculation as above for $\langle \epsilon_\delta(r_n)^q \rangle$ yields $D_\delta(q) \equiv 0, q > 0$; so we again find monoscaling. In particular, we have $D_f(S) = 0$, meaning that the measure is entirely concentrated onto a single point.

A stochastic multiscaling example: We repeat the above procedure simply by changing the multiplicative weights (denoted W) from 0 and 2 to $2p$ and $2(1 - p)$, $0 \leq p \leq 1/2$, yielding $\epsilon_p(r_n; x)$. This so-called p model (Meneveau and Sreenivasan 1987b) is illustrated in Fig. A2 on a log scale for $p = 0.3$ and $n = 10$. All realizations of the field $\epsilon_p(r_n; x)$ have the same n th-order binomial distribution of values: $\epsilon_i^{(n)}(p) = (2p)^i (2 - 2p)^{n-i}$ with probability $\binom{n}{i} / 2^n$ for $i = 0, \dots, n$. As n increases, more positively skewed log-binomial distributions arise that maintain $\langle \epsilon_p(r_n) \rangle \equiv 1$ for all n . The box-counting algorithm described in connection with Eq. (A1) can be applied to the level set $L_i(p, n) = \{x \in [0, 1], \epsilon_p(r_n; x) = \epsilon_i^{(n)}(p)\}$ with $n \gg 1$, at least for scales $r \geq r_n$; Fig. A2 shows that different values of $D_f[L_i(p, n)]$ will be obtained for different i . These fractal dimensions range from 1 (space-filling) at the most probable level $i = n/2$ to 0 (single points) for $i = 0, n$. The associated field $\epsilon_p(r_n; x)$ is called multifractal. Halsey et al. (1986) show how a Legendre transform can be used to obtain the multiple fractal dimensions from the $D(q)$ hierarchy, equivalently $K(q)$. For the p model we have $K_p(q) = \log_2 \langle W^q \rangle = \log_2 [(2p)^q / 2 + (2 - 2p)^q / 2]$, hence

$$D_p(q) = \frac{-1}{q - 1} \log_2 [p^q + (1 - p)^q], \tag{A4}$$

for any q (as long as $0 < p \leq 1/2$). This is a case of multiscaling since many exponents are needed to describe the statistics; in particular, we can extract from the hierarchy $D_p(q)$

- $D_p(-\infty) = -\log_2 p > 1$;
- $D_p(0) = 1$ (as long as $p > 0$) is the “capacity” dimension;



$$D_{g(\varphi)} = 2 - H_1, \tag{A6}$$

FIG. A2. Log-binomial multifractal measure on a log scale. Meneveau and Sreenivasan's (1987b) p model $\epsilon_p(r_n; x)$ with $n = 10$ cascade steps ($1/r_n = 2^n = 1024$ grid points) and $p = 0.3$. On either side of the mean $\langle \epsilon \rangle = 1$ level, we indicate the most probable level $\epsilon_{mp} = 2^n [p^i(1-p)^{n-i}]$ with $i = n/2$ and the one that contributes most to the mean, namely $\epsilon_1 = 2^n [p^i(1-p)^{n-i}]$ with $i = np$; in this case, we have $\epsilon_{mp} \approx 0.42$ and $\epsilon_1 \approx 2.3$. The dimension of the level set of ϵ_{mp} is unity: it fills the interval. For ϵ_1 , we find a smaller (fractal) value: $D_{0.3}(1) = -0.3 \log_2 0.3 - 0.7 \log_2 0.7 \approx 0.88$, the information dimension; notice that $\epsilon_1 = r_n^{2.3(1)-1} = r_n^{-0.7}$.

- $D_p(1) = -[p \log_2 p + (1-p) \log_2 (1-p)] < 1$ is the "information" dimension, hence $C_1(p) = 1 - D_p(1)$;
- $D_p(2) = -\log_2 [1 - 2p(1-p)] < D_1(p)$ is the "correlation" dimension; and
- $D_p(\infty) = -\log_2 (1-p) < D_2(p)$.

There are two monoscaling limits for this tutorial model: a trivial one for $p \rightarrow 1/2^-$ that leads to flat fields, $K_{1/2}(q) \equiv 0$ and $D_{1/2}(q) \equiv 1$ for all q , and a nontrivial one for $p \rightarrow 0^+$ that leads to δ functions, $K_{0^+}(q) \equiv q - 1$ and $D_{0^+}(q) \equiv 0$ for $q > 0$.

b. From self-affine graphs to multiaffine random processes

Of all the scaling structure functions in Eq. (4), the first-order case

$$\langle |\varphi(x+r) - \varphi(x)| \rangle \sim r^{H_1}, \quad H_1 = \zeta(1) \tag{A5}$$

has attracted a lot of attention but under a rather different guise. Indeed, it is related to the fractal dimension $D_{g(\varphi)}$ of the graph of $\varphi(x)$, viewed as a random self-affine geometrical object "g(φ)" in two-dimensional space (Mandelbrot 1977; Falconer 1990; Higuchi 1988). It can be shown that definitions (A1) and (A5) lead to

which necessarily lies between unity (a rectifiable curve) and two (a measurable area), inclusive. The codimension of $g(\varphi)$, $2 - D_{g(\varphi)} = H_1$, can go from zero to unity and thus provides a direct and natural measure of smoothness; $D_{g(\varphi)} - 1 = 1 - H_1$ is a measure of roughness. Furthermore, the recent introduction of the "cancellation exponent" κ in the physics and turbulence literature has generated new interest in the roughness and/or nonstationarity properties described by H_1 ; indeed, $\kappa = 1 - H_1$ is used to describe the rate at which the fluctuations of $\varphi(x)$ change direction, equivalently, how often a "signed" measure, meaning essentially the derivative of $\varphi(x)$, changes sign (Ott et al. 1992; Vainshtein et al. 1994; Bertozzi and Chhabra 1994).

Illustration with monoscaling random functions: Stationary scaling processes have scale-independent increments ($H_1 = 0$) and their graphs fill space ($D_{g(\varphi)} = 2$); this is true for white noise, $1/f$ noise (Fig. 11, upper curve), and all multiplicative cascades (e.g., Fig. 12). Space-filling graphs are a geometrical consequence of the characteristic discontinuity of these processes, discussed in Part I. The H_1 values chosen for fBm in Fig. 11 are $1/3$ in the rougher case, $D_{g(\varphi)} = 5/3$, and $2/3$ in the smoother case, $D_{g(\varphi)} = 4/3$. Graphs of standard Bm with $H_1 = 1/2$, such as the intermediate case in Fig. 11, have fractal dimension $3/2$. Random linear trends and Heaviside steps were introduced in section 4b as extreme examples of nonstationary behavior; they are equally smooth, being almost everywhere differentiable, so $D_{g(\varphi)}$ is unity in both cases, leading to $H_1 = 1$.

The cases of fBm discussed above constitute a very special kind of statistical self-affinity. They are best referred to as "monoaffine," adopting Viscek and Barabási's (1991) expression "multiaffinity" for the more geophysically relevant situations where $\zeta(q)$ is not linear in q .

Multiscaling random functions, a brief survey: Despite its direct relevance to data, multiaffine modeling, with controllable values of H_1 in particular, is only beginning. Barabási and Vicsek (1991) describe a variant of the midpoint displacement algorithm for fBm used in Fig. 11 that yields a multiscaling random function; Arnéodo et al. (1993) use integrals of multiplicative cascades with negative weights to obtain the same effect. Aurell et al. (1992) show that the solutions of Burger's equation have $\zeta(q) = \min\{q, 1\}$. Benzi et al. (1993) describe a wavelet-based algorithm that delivers a random process with any prescribed $\zeta(q)$. In order to model the multiscaling properties of an admixture in a turbulent plume, Sykes et al. (1995) use a standard multiplicative cascade to modulate the scale-dependent variances in a midpoint displacement procedure. At least two early models have proved to be multiaffine. Schertzer and Lovejoy (1987) propose multiplicative cascades and "fractional" integration of order $0 < H < 1$. Cahalan et al.'s (1994a) "bounded" cascade models (used

to illustrate nonstationarity in Part I) generalize the singular p models (discussed above) simply by making the multiplicative weights tend to unity as the cascade proceeds; they have $\zeta(q) = \min\{qH, 1\}$ with $H > 0$ being a smoothing parameter (Marshak et al. 1994). These two last multifractal models were originally developed to simulate clouds with realistic internal distributions of LWC.

The fractal geometrical interpretation of $\zeta(q)$ using local Hölderian properties and Legendre transforms is outside the scope of this introduction; the interested reader is referred to the seminal paper by Parisi and Frisch (1985), the first to use the term multifractal.

REFERENCES

- Albrecht, B. A., D. A. Randall, and S. Nicholls, 1988: Observations of marine stratocumulus clouds during FIRE. *Bull. Amer. Meteor. Soc.*, **69**, 618–626.
- , C. S. Bretherton, D. Johnson, W. H. Schubert, and A. S. Frisch, 1995: The Atlantic Stratocumulus Transition Experiment—ASTEX. *Bull. Amer. Meteor. Soc.*, **76**, 889–904.
- Arnéodo, A., J.-F. Muzy, and E. Bacri, 1992: Wavelet analysis of fractal signals. Applications to fully developed turbulence data. *Eddy Structure Identification in Free Turbulent Shear Flows*, J. P. Bonnet and M. N. Glauser, eds., Kluwer, 153–158.
- Aurell, E., U. Frisch, J. Lutsko, and M. Vergassola, 1992: On the multifractal properties of the energy dissipation derived from turbulence data. *J. Fluid Mech.*, **238**, 467–486.
- Barabási, A.-L., and T. Viscek, 1991: Multifractality of self-affine fractals. *Phys. Rev. A*, **44**, 2730–2733.
- Barker, H. W., and J. A. Davies, 1992: Cumulus cloud radiative properties and the characteristics of satellite radiance wavenumber spectra. *Remote Sens. Environ.*, **42**, 51–64.
- Benzi, R., L. Biferale, A. Crisanti, G. Paladin, M. Vergassola, and A. Vulpani, 1993: A random process for the construction of multi-affine fields. *Physica D*, **65**, 352–358.
- Bertozzi, A. L., and A. B. Chhabra, 1994: Cancellation exponents and fractal scaling. *Phys. Rev. E*, **49**, 4716–4719.
- Cahalan, R. F., 1989: Overview of fractal clouds. *Advances in Remote Sensing and Retrieval Methods*, A. Deepak, H. Fleming, and J. Theon, Eds., Deepak, 371–388.
- , and J. B. Snider, 1989: Marine stratocumulus structure. *Remote Sens. Environ.*, **28**, 95–107.
- , W. Ridgway, W. J. Wiscombe, T. L. Bell, and J. B. Snider, 1994a: The albedo of fractal stratocumulus clouds. *J. Atmos. Sci.*, **51**, 2434–2455.
- , —, —, S. Golmer, and Harshvardhan, 1994b: Independent pixel and Monte Carlo estimates of stratocumulus albedo. *J. Atmos. Sci.*, **51**, 3776–3790.
- Chhabra, A. B., C. Meneveau, R. V. Jensen, and K. R. Sreenivasan, 1989: Direct determination of the $f(\alpha)$ singularity spectrum and its application to fully developed turbulence. *Phys. Rev. A*, **40**, 5284–5294.
- Christakos, G., 1992: *Random Fields in Earth Sciences*. Academic Press, 474 pp.
- Davis, A., P. Gabriel, S. Lovejoy, D. Schertzer, and G. Austin, 1990: Discrete angle radiative transfer. III. Numerical results and meteorological applications. *J. Geophys. Res.*, **95**, 11 729–11 742.
- , S. Lovejoy, and D. Schertzer, 1991a: Radiative transfer in multifractal clouds. *Scaling, Fractals and Nonlinear Variability in Geophysics*, S. Lovejoy and D. Schertzer, Eds., Kluwer, 303–318.
- , —, and —, 1991b: Discrete angle radiative transfer in multifractal medium. *S.P.I.E. Proc.*, **1558**, 37–59.
- , A. Marshak, and W. Wiscombe, 1993: Bi-multifractal analysis and multi-affine modeling of non-stationary geophysical processes, application to turbulence and clouds. *Fractals*, **1**, 560–567.
- , —, —, and R. Cahalan, 1994a: Multifractal characterizations of non-stationarity and intermittency in geophysical fields, observed, retrieved or simulated. *J. Geophys. Res.*, **99**, 8055–8072.
- , —, and —, 1994b: Wavelet-based multifractal analysis of non-stationary and/or intermittent geophysical signals. *Wavelets in Geophysics*, E. Foufoula-Georgiou and P. Kumar, Eds., Academic Press, 249–298.
- , —, —, and R. Cahalan, 1996a: Scale-invariance in liquid water distributions in marine stratocumulus. Part I: Spectral properties and stationarity issues. *J. Atmos. Sci.*, **53**, 1538–1558.
- , —, —, and —, 1996b: Multifractal characterizations of intermittency in nonstationary geophysical signals and fields—A model-based perspective on ergodicity issues illustrated with cloud data. *Current Topics in Nonstationary Analysis*, G. Trevisño, Ed., World-Scientific, 97–158.
- , —, R. Cahalan, and W. Wiscombe, 1997: The Landsat scale break in stratocumulus as a three-dimensional radiative transfer effect, implications for cloud remote sensing. *J. Atmos. Sci.*, **54**, 241–260.
- Eneva, M., 1994: Monofractal or multifractal: A case study of spatial distribution of mining induced seismic activity. *Nonlinear Processes Geophys.*, **1**, 182.
- Evans, K. F., 1993a: Two-dimensional radiative transfer in cloudy atmospheres: The spherical harmonic spatial grid method. *J. Atmos. Sci.*, **50**, 3111–3124.
- , 1993b: A general solution for stochastic radiative transfer. *Geophys. Res. Lett.*, **20**, 2075–2078.
- Falconer, K. J., 1990: *Fractal Geometry—Mathematical Foundations and Applications*. Cambridge University Press, xxii+281 pp.
- Frisch, U., 1991: From global scaling, à la Kolmogorov, to local multifractal in fully developed turbulence. *Proc. Roy. Soc. London, ser. A*, **434**, 89–99.
- Gabriel, P., S. Lovejoy, D. Schertzer, and G. Austin, 1988: Multifractal analysis of resolution dependence in satellite imagery. *Geophys. Res. Lett.*, **15**, 1373–1376.
- , —, A. Davis, D. Schertzer, and G. Austin, 1990: Discrete angle radiative transfer. II. Renormalization approach for homogeneous and fractal clouds. *J. Geophys. Res.*, **95**, 11 717–11 728.
- Grassberger, P., 1983: Generalized dimensions of strange attractors. *Phys. Rev. Lett. A*, **97**, 227–330.
- Gupta, V. K., and E. C. Waymire, 1993: A statistical analysis of mesoscale rainfall as a random cascade. *J. Appl. Meteor.*, **32**, 251–267.
- Halsey, T. C., M. H. Jensen, L. P. Kadanoff, I. Procaccia, and B. I. Shraiman, 1986: Fractal measures and their singularities: The characterization of strange sets. *Phys. Rev. A*, **33**, 1141–1151.
- Hentschel, H. G. E., and I. Procaccia, 1983: The infinite number of generalized dimensions of fractals and strange attractors. *Physica D*, **8**, 435–444.
- Higuchi, T., 1988: Approach to an irregular time series on the basis of the fractal theory. *Physica D*, **31**, 277–283.
- Kahane, J.-P., and J. Perrière, 1976: Sur certaines martingales de Benoit Mandelbrot. *Adv. Mathematics*, **22**, 131–145.
- Kolmogorov, A. N., 1941: Local structure of turbulence in an incompressible liquid for very large Reynolds numbers. *Dokl. Akad. Nauk SSSR*, **30**, 299–303.
- , 1962: A refinement of previous hypothesis concerning the local structure of turbulence in viscous incompressible fluid at high Reynolds number. *J. Fluid Mech.*, **13**, 82–85.
- Lau, K.-M., and H. Weng, 1995: Climate signal detection using wavelet transform. *Bull. Amer. Meteor. Soc.*, **76**, 2391–2401.
- Lavallée, D., S. Lovejoy, and D. Schertzer, 1991: On the determination of the codimension function. *Non-linear Variability in Geophysics*, D. Schertzer and S. Lovejoy, Eds., Kluwer, 99–110.
- , —, —, and P. Ladoy, 1993: Nonlinear variability and sim-

- ulation of landscape topography. *Fractal in Geography*, L. De Cola and M. Lam, Eds., Kluwer, 158–192.
- Mandelbrot, B. B., 1974: Intermittent turbulence in self-similar cascades: Divergence of high moments and dimension of the carrier. *J. Fluid Mech.*, **62**, 331–358.
- , 1977: *Fractals: Form, Chance, and Dimension*. W. H. Freeman, 365 pp.
- Marshak, A., A. Davis, R. Cahalan, and W. Wiscombe, 1994: Bounded cascade models as non-stationary multifractals. *Phys. Rev. E*, **49**, 55–69.
- , —, W. Wiscombe, and G. Titov, 1995a: The verisimilitude of the independent pixel approximation used in cloud remote sensing. *Remote Sens. Environ.*, **52**, 72–78.
- , —, and —, 1995b: Radiation smoothing in fractal clouds. *J. Geophys. Res.*, **100**, 26 247–26 261.
- Meneveau, C., and K. R. Sreenivasan, 1987a: The multifractal spectrum of the dissipation field in turbulent flows. *Nucl. Phys. B*, **2**, 49–76.
- , and —, 1987b: Simple multifractal cascade model for fully developed turbulence. *Phys. Rev. Lett.*, **59**, 1424–1427.
- , and —, 1989: Measurements of $f(\alpha)$ from scaling of histograms, and applications to dynamical systems and fully developed turbulence. *Phys. Lett. A*, **137**, 103–112.
- Monin, A. S., and A. M. Yaglom, 1975: *Statistical Fluid Mechanics*. Vol. 2. MIT Press, 683 pp.
- Muzy, J.-F., E. Bacry, and A. Arnéodo, 1993: Multifractal formalism for fractal signals: The structure-function approach versus the wavelet-transform modulus-maxima methods. *Phys. Rev. E*, **47**, 875–884.
- , —, and —, 1994: The multifractal formalism revisited with wavelets. *Int. J. Bifurcation Chaos*, **4**, 245–302.
- Obukhov, A., 1962: Some specific features of atmospheric turbulence. *J. Fluid Mech.*, **13**, 77–81.
- Ott, E., 1993: *Chaos in Dynamical Systems*. Cambridge University Press, 385 pp.
- , Y. Du, K. R. Sreenivasan, A. Juneja, and A. K. Suri, 1992: Sign-singular measures: Fast magnetic dynamos, and high Reynolds-number fluid turbulence. *Phys. Rev. Lett.*, **69**, 2654–2657.
- Parisi, G., and U. Frisch, 1985: A multifractal model of intermittency. *Turbulence and Predictability in Geophysical Fluid Dynamics*, M. Ghil, R. Benzi, and G. Parisi, Eds., North Holland, 84–88.
- Schertzer, D., and S. Lovejoy, 1987: Physical modeling and analysis of rain clouds by anisotropic scaling multiplicative processes. *J. Geophys. Res.*, **92**, 9693–9714.
- , and —, 1992: Hard and soft multifractal processes. *Physica A*, **185**, 187–194.
- Schmitt, F., D. Lavallée, D. Schertzer, and S. Lovejoy, 1992: Empirical determination of universal multifractal exponents in turbulent velocity fields. *Phys. Rev. Lett.*, **68**, 305–308.
- Sreenivasan, K. R., 1991: Fractals and multifractals in fluid turbulence. *Annu. Rev. Fluid Mech.*, **23**, 539–600.
- Sykes, R. I., R. S. Gabruk, and D. S. Henn, 1995: A multifractal representation of the small-scale structure in a turbulent plume. *J. Appl. Meteor.*, **34**, 2294–2305.
- Tessier, Y., S. Lovejoy, and D. Schertzer, 1993: Universal multifractals: Theory and observations for rain and clouds. *J. Appl. Meteor.*, **32**, 223–250.
- Vainshtein, S. I., K. R. Sreenivasan, R. T. Pierrehumbert, V. Kashyap, and A. Juneja, 1994: Scaling exponents for turbulence and other random processes and their relationships with multifractal structure. *Phys. Rev. E*, **50**, 1823–1835.
- Viscek, T., and A.-L. Barabási, 1991: Multi-affine model for the velocity distribution in fully turbulent flows. *J. Phys. A: Math. Gen.*, **24**, L845–L851.
- Waymire, E., and V. J. Gupta, 1981: The mathematical structure of rainfall representations. I. A review of the stochastic rainfall models. *Water Resour. Res.*, **17**, 1261–1272.